Microparticle Swarms - Faster Together

The Effect of Particle Concentration on Colloidal Transport in Fractured and Porous Media

Pierrick Spekreijse

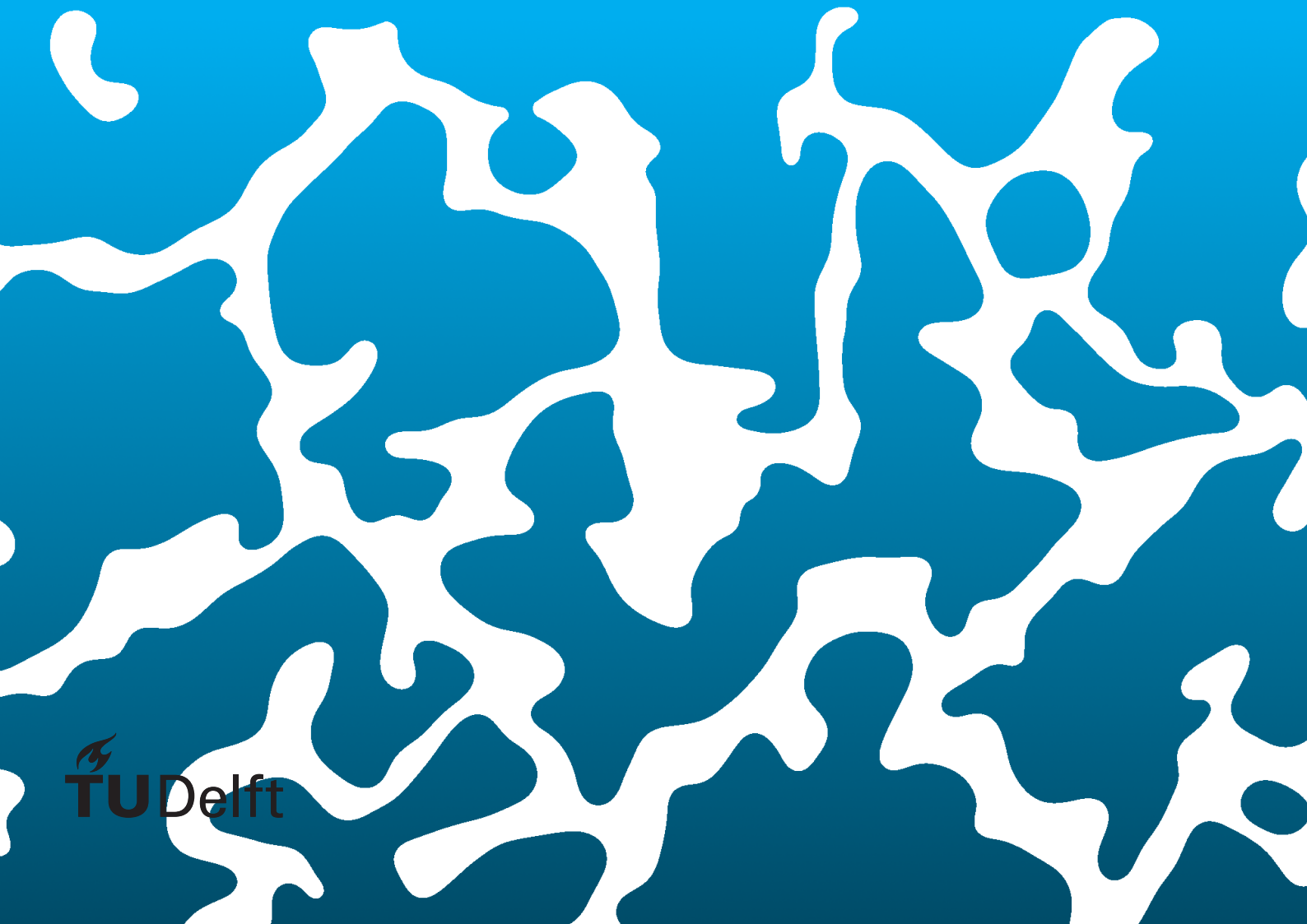

TU Delft

Microparticle Swarms - Faster Together

The Effect of Particle Concentration on Colloidal Transport in Fractured and Porous Media

by

Pierrick Spekreijse

to obtain the degree of Master of Science
at the Delft University of Technology,
to be defended publicly on December 17, 2021 at 13:00.

Student number: 4569288

Project duration: Februari 8, 2021 – December 17, 2021

Thesis committee:

Dr. T. A. Bogaard,	TU Delft, supervisor
Dr. J. W. Foppen,	IHE Delft - TU Delft
Dr. C. Chassagne,	TU Delft
B. Kianfar, MSc	TU Delft

TU Delft

Preface

This thesis was written to obtain the degree of Master of Science at the Delft University of Technology. It is especially interesting to experts concerned with colloidal particle transport processes and more specifically, the formation and behaviour of colloidal particle swarms. Those interested in trajectory analysis, particle concentration determination based on video footage, x-ray data analysis in Python and conversion of real materials to 3D printed samples may find useful techniques in Chapter 2.

I would like to express my deepest gratitude to Dr. T. A. Bogaard, whose supervision and optimism have guided me through the graduation process. His keen interest and curiosity have made writing this thesis a pleasure. My appreciation also goes out to Dr. J. W. Foppen for his critical view and forthrightness, which have been greatly beneficial to my work. In addition, I would like to thank Dr. C. Chassagne for her help and input with the modelling process and Ms. Kianfar for her suggestions and energy and enthusiasm while helping me in the laboratory. I thank profusely the staff of the WaterLab for assisting me in securing a lab space and providing the necessary tools and materials. I would also like to thank family and friends for proofreading my thesis and providing me with their insights on substance, readability and layout. A final note of appreciation goes out to my friend, Tom Edixhoven, for his invaluable recommendations and improvements in my Python code.

Pierrick Spekreijse
Delft, December 2021

Abstract

Colloidal particle swarms can show settling velocities over a thousand times as fast as that of a single particle. The transport of colloidal particles is thus strongly affected by the formation and behaviour of these particle swarms, which could have important implications for the widespread use and prevalence of colloidal particles. Swarming effects may for example pose possibilities and limitations to the use of (colloidal) DNA tracers in various systems. Furthermore, contaminant transport in blue-green porous infrastructure may be greatly enhanced due to the rapid settling of swarms of colloidal contaminants, resulting in rapid spreading of contaminants into the environment.

To better understand colloidal particle swarms in these systems, this thesis studied the effect of particle concentration on the behaviour of colloidal swarms in varying confining geometries.

To this extent, colloidal particles were injected at various concentrations in a macro-model that was suspended in a stagnant water column. The macro-model consisted of three different artificial confining geometries: a smooth fracture, a rough fracture and a pore network. Released swarms were imaged to determine their velocity, width, travelled distance to bifurcation and particle leakage rates from the swarm. In the smooth and rough fracture, the settling velocity of colloidal particle swarms was modelled with the Hadamard & Rybczynski (HR) equation, using the particle leakage rate of the swarm. The average swarm velocity in the pore network was modelled with equations that described the Boycott effect.

In both the smooth and rough fracture, the average velocity of the swarm showed a slight decreasing trend with increasing particle concentration. Presumably, this was caused by the linear relationship between particle concentration and width of the swarm. Consequently, wider swarms experienced lower velocities due to increased hydrodynamic drag forces imposed on the swarm. In the pore network, a strong linear relation was found between the average swarm velocity and the particle concentration. A larger mass of the swarm may have been the cause for this. The travelled distance before bifurcation took place did not show a clear relationship with particle concentration. However, in the performed experiments, swarms did bifurcate at a threshold width in both the smooth and rough fracture. This threshold width increased with concentration.

The HR model did not fit the swarm velocity in the smooth fracture well, because confining forces of the fracture walls enhanced swarm velocity, which was not accounted for by the HR model. Yet, in the rough fracture the HR model did fit well to the observed swarm velocity since the increased drag forces of wall on the swarm counteracted the confining forces. The effect of particle concentration on the average swarm velocity in the pore network was sufficiently well modelled in terms of the Boycott effect.

It was recommended that in future studies laminar flow is introduced to enable better interpretation of results for natural systems. In addition, a more simple pore network geometry provides a more gradual transition to the used complex pore network geometry. This would allow for clearer investigation of swarm behaviour in porous media. Also, more research on swarm behaviour after bifurcation may provide more insight in the longevity of swarm effects.

To determine if colloidal particle swarms may occur in natural fractured media, results of this study should be compared to a field study. Both physical and chemical disturbances may severely hinder colloidal swarms. For both fractured and porous media, injection into a natural sample may provide more insight in behaviour in natural systems. It is however unlikely that swarming effects play a big role in urban colloidal contaminant transport in porous media.

Contents

1 Introduction

1.1. Background

There are many suspended particles in natural and wastewater systems; particles with a diameter smaller than $10\ \mu m$ are generally defined as colloids (McCarthy and Zachara, 1989; Stumm, 1977). Colloid retention and transport processes have been a subject of study in the past decades (Molnar et al., 2015), with a growing interest since the foundation has been laid out in colloid filtration theory (CFT) (Yao et al., 1971). Much research has since been done on colloid transport in preferential flow paths in porous media, which can hugely enhance transport rates. (Bradford et al., 2004; Kjaergaard et al., 2004; Leij and Bradford, 2013; Mohanty et al., 2016; Saiers et al., 1994).

Recently, another mechanism that can greatly increase colloidal transport rates has been investigated. The occurrence of particles moving as a swarm in porous media and fractures has been demonstrated (Boomsma and Pyrak-Nolte, 2015; Molnar et al., 2019). These particles settle under gravity and fluid inertia is negligible. A particle swarm can be seen as an effective continuum with a larger density than that of the surrounding fluid, remaining a cohesive entity for a long time. The swarm maintains a clear boundary between the particles that recirculate on the inside and the surrounding fluid, despite the absence of surface tension at the drop surface (Metzger et al., 2007; Myłyk et al., 2011; Nitsche and Batchelor, 1997). A key characteristic of a colloidal particle swarm is that its settling velocity is significantly higher than the Stokes single particle settling velocity:

$$v_0 = \frac{1}{18}\frac{(\rho_p - \rho_f)ga^2}{\mu} \tag{1.1}$$

In which v_0 is the single particle settling velocity $[m/s]$, ρ_p and ρ_f the density of the particle and fluid respectively $[kg/m^3]$, g the gravitational constant $[m/s^2]$, a the particle diameter $[m]$ and μ the dynamic viscosity $[kg/(m*s)]$.

The development of a particle swarm in unconfined conditions has been studied by multiple authors (Adachi et al., 1978; Grace, 1971; Metzger et al., 2007; Nitsche and Batchelor, 1997; Stone, 1994), but the work of Machu et al. (2001) has most elaborately described the evolution of such swarms. Upon injection of the suspension of particles, a bell-shaped swarm forms where the rear is an elongated conical shape as result of the injection process; the swarm somewhat resembles a reversed mushroom cloud (Figure 1.1, left). It should be noted that some authors find a more spherical shape (Boomsma and Pyrak-Nolte, 2015; Nitsche and Batchelor, 1997), although Myłyk et al. (2011) had to use a specially design drop injector for this purpose. As the swarm progresses through the fluid medium, liquid is entrained at the upper part of the drop, which then starts to circulate. Entrainment of fluid leads to formation a ring-like structure, that is often referred to as a *torus* (Figure 1.1, right). At this point, the torus is still a *closed* torus, meaning that the streamlines run outside the torus. At the rear, the recirculating streamlines lead to the ejection of particles from the center of the swarm. However, at some point, the torus evolves into a *open* torus, meaning that the streamlines pass through the ring. The open torus is unstable and at some point bifurcates into two or more smaller swarms. This process then repeats itself. Throughout this evolution, particles can randomly cross the boundary of the suspension drop, where the streamlines transport them to the rear of the drop, where it is ejected and forms a tail. The tail represents the travelled path of a drop and shows the history of its location in time.

Figure 1.1: Different stages of drop evolution, swarm consists of glass particles in glycerin. Taken from (Machu et al., 2001).

While the observation and studying of suspension drops is thus not new, application of swarm theory to fractures and porous media is one of the latest developments in the field. Swarming effects of colloidal particles can influence their transport rates, as these swarms are able to travel much faster than a single particle. Molnar et al. (2019) reports that the settling velocity of a swarm in a dilute solution under gravity can theoretically be as much as 10,000 times the settling velocity of an individual particle. Gravity driven swarm behaviour in fractures is different, as the fracture walls influence the cohesiveness and velocity of the swarm. Crucial to the transport of a swarm through a fracture is the ratio of fracture aperture to swarm diameter. There exists an optimal ratio in which drag on the swarm is small and cohesiveness of the swarm is promoted. Boomsma and Pyrak-Nolte (2015) found that in fractures with optimal aperture, swarms could travel 1000 times as fast as the settling velocity of a single particle. With these experiments in fractures, it becomes even more evident that particle swarms cannot be seen as many single particles. Happel and Brenner (1965) present the following equation for the drag force on a single particle between two parallel walls:

$$F = \frac{-6\pi\mu a v_p}{1 - 1.004(\frac{a}{d}) + 0.418(\frac{a}{d})^3 + 0.21(\frac{a}{d})^4 - 0.169(\frac{a}{d})^5} \tag{1.2}$$

With v_p the velocity of a single settling particle and d the distance of the particle from the wall.

Boomsma and Pyrak-Nolte (2015) showed that a single particle should not be affected by fracture walls, since the effect of the walls is negligible around $\frac{a}{d} \approx 0.1$ and in their experiments, $\frac{a}{d} \approx 0.001 << 0.1$. However, their results clearly indicate an effect of fracture walls and geometry. Single particle equations can thus not describe the behaviour of colloidal particle swarms.

It is clear that colloid transport is strongly affected by the formation and behaviour of colloidal particle swarms. This may have important implications for the widespread use and prevalence of colloidal particles. An example of such use of colloids is the application of DNA tracers, which have a low detection sensitivity and allows for multipoint detection by creating DNA "labels" for each source location (Liao et al., 2018; Sharma et al., 2012; Tang et al., 2021). These tracers have a DNA core, encapsulated by a silica layer (Paunescu et al., 2013), and their microscopic size makes them a colloidal particle. The transport rates of these particles can be different from the fluid in which it travels due to swarming effects, which could pose possibilities and limitations to use of such tracers.

Swarming effects of colloids can also affect contaminant transport in urban blue-green infrastructure. Colloids seem to play an important role in the transport of heavy metals and organic compounds and colloids may actually be a large fraction of the present (heavy) metals in stormwater runoff (Grout et al., 1999). Key to many of the blue-green water management and retention solutions in urban areas is the high porosity to facilitate rapid stormwater infiltration. However, colloidal swarms may result in even faster transport of colloidal contaminants into the environment.

The rapid transport behaviour of colloidal swarms can thus lead to problems as described above. Colloidal swarms in porous media and in fractures have been observed, but the effect of particle concentration is not yet fully explored. To better understand colloid transport and consequently the applications in which colloidal particles are involved, it is necessary to examine the effect of initial particle concentration on colloidal swarm behaviour in confining geometries.

1.2. Research question

The proposed research question therefore is the following: *What is the effect of particle concentration on the behaviour of colloidal swarms in varying confining geometries?*

1.3. Method and boundary conditions

The optimal fracture regime was firstly analysed to ensure suitable conditions for colloidal swarm transport in fractures, as based on Boomsma and Pyrak-Nolte (2015). They suggest that an optimal fracture aperture exists in which tangential drag of the wall is minimized and confining forces to prevent swarm bifurcation is optimized. Preparatory experiments were therefore firstly performed with a uranine and salt solution to investigate the aperture confinement range.

Secondly, the experiments of Boomsma and Pyrak-Nolte (2015) on smooth fractures were reproduced with colloidal particles. Then, an attempt was made to expand their findings on rough fractures by using a 3D printed clay fracture. It is hypothesized that colloidal swarms experience large confining forces and small tangential forces while travelling in a fracture, where the rough fracture should impose larger tangential forces on the swarm than the smooth fracture. In the pore network, tangential forces are increased due to a decreased distance of the swarm to the wall. Experiments were thus performed with increasing complexity regarding the geometry of the environment and its corresponding tangential forces.

Thirdly, when more knowledge and experience had been gained on creating swarms, it was studied if particle swarms can also be expected in porous media and if there are particular concentrations of colloids for which swarming effects in porous media are not to be expected. In these experiments, custom made 2D pore networks were constructed and printed.

Finally, simple, first order modelling was applied to give more insight in the effect of concentration on colloidal swarms in both smooth and rough fractures, as well as a pore network.

This proposed study particularly evaluates the effect of a varying particle concentration and geometry on colloidal swarm transport. Although it is known that more factors, such as particle spacing from the wall, particle diameter, volume, drop size and density affect swarm behaviour, these factors are not examined in this study. In addition, the scope of this study is limited to fractured and porous media. The effects of flow velocity are acknowledged (Adachi et al., 1978; Lin et al., 2017; Machu et al., 2001; Malenda and Pyrak-Nolte, 2016) but not further evaluated.

Chapter 2 describes the applied experimental methods. The used theoretical models are elaborated upon in chapter 3 Chapter 4 presents and discusses the experimental and modelling results. Conclusions and recommendations are put forward in Chapter 5.

2

Methodology

As previously discussed, experiments were performed in artificial fractures and porous media. To test the artificial samples, a macro-model was constructed. The macro-model consisted of a see-through acrylic block and an interchangeable, non see-through block which contained the surface subject to testing (i.e. a smooth fracture, a rough fracture and a pore network). The general experimental setup is discussed in section 2.2. The interchangeable blocks of the macro-model are discussed in separate sections thereafter. The experimental setup was largely based on the work of Boomsma and Pyrak-Nolte (2015) and Boomsma (2014), who have studied particle swarming effects in fractures. The majority of experiments have been performed in triplicate.

2.1. Colloidal particles

The colloidal particles used were fluorescent polystyrene beads (R0300B, Thermo Fisher) with a (metric) mean particle diameter of $3.2\ \mu m$ and a particle density of $1.05\ g/cm^3$. The stock solution had a mass concentration of 1 %. The excitation wavelength of these particles was $542\ nm$ (green-blue) and the emission wavelength was $612\ nm$ (red). The particle density was determined by counting a 100 times diluted stock solution in a Neubauer chamber (Figure A.1, Appendix A) and was determined to be $650,000$ particles/μL.

Before further handling of the particle solution, the particles were washed to remove the surfactant, since the surfactant may alter drop shape and surfactant gradients may lead to fluid motion (Stone, 1994). The solution was centrifuged at 13400 RPM for 2 minutes (MiniSpin, Eppendorf), after which the supernatant was carefully pipetted out. Deionized water was then added to the Eppendorf microtube, up to $1\ mL$. This process was repeated three times. To determine whether the particles were stable in the solution, the zeta potential was measured (Zetasizer, Malvern Panalytical). A measured zeta potential of $-37.3\ mV \pm 3.81$ indicated stability of the washed particles in solution (Malvern Instruments Ltd, 2021). The hydrodynamic diameter could also be measured in the Zetasizer and was $4952\ nm \pm 576.6$ (also see Appendix A).

The washed solution was used to create particle suspensions of 0.5, 1, 2, 3.5 and 5% by mass. Boomsma and Pyrak-Nolte (2015) proposed that particle swarming occurs in the $1-4$ % range, so a concentration range from 0.5 to 5 % allowed examination of the effect of initial particle concentration (c_0) on swarming effects in artificial fractures and porous media.

The washed stock solution at 1% was centrifuged at 13400 RPM for 2 minutes, after which the required amount of supernatant could be removed to create a new solution of 5%. This solution could then be step-wise diluted to create the required concentrations. The diluted samples were thus further diluted until the 0.5% concentration was achieved. This ensured that the ratio of these dilutions were accurate, despite possible errors in the creation of the 5% solution.

2.2. Experimental setup

A macro-model was constructed, consisting of a see-through acrylic block ($103\,mm * 103\,mm * 20\,mm$) and an equally sized block containing the surface subject to testing, which was either a second smooth acrylic block, a 3D printed clay fracture wall or a 3D printed pore network (Figure 2.1). The two blocks of the macro-model were joined by two M5 bolts, placed $1.5\ cm$ from both the side and the top of the block. By twisting the bolts, the fracture aperture could be set. A thin nylon cord was used to hang the macro-model in a large wooden tank ($75\ cm\ *\ 30\ cm\ *\ 23\ cm$), along which it could also be moved to ensure a level positioning. The front side of the tank was made of glass, such that the inside of the tank could be seen. The height of the tank allowed used particles to sink to the bottom, where they were of no hindrance and remained during the remainder of the other experiments. The water in the tank was changed between series of experiments, i.e. after the $1-5\ \%$ injections in the smooth fracture, rough fracture and pore network.

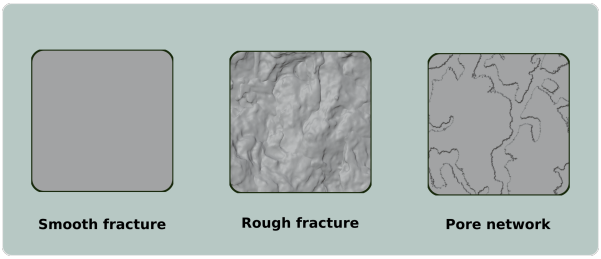

Figure 2.1: Schematic representation of the various surfaces that were tested in the macro-model

The tank was filled with deionized water until the water level was well above the macro-model, approximately $25\ mm$ below the top of the tank. This allowed injection of colloidal suspension $1.5\ cm$ below the top of the macro-model, using a 23G hypodermic needle ($0.6 * 25 mm$). The created solutions, 0.5, 1, 2, 3.5 and $5\ \%$ by mass, were injected in the macro-model. The concentration of the colloidal suspension was varied, whilst injection volume was kept constant at approximately $9.5\ \mu L$. Variation in concentration enabled evaluation of the effect of particle concentration on colloidal swarm behaviour. A mechanical syringe pump (ProSense NE-1010) was used to release the swarms at a rate of $1\,mL/min$. A series of LED lights emitting a green-yellow colour was placed on the glass side of the tank in order to excite the fluorescent particles. Tracing paper was placed between the LEDs and the glass to ensure a more homogeneous, diffuse lighting environment. A video camera (Canon Legria HF S20) was used to observe the particles as they moved through the macro-model. The camera filmed with 25 frames per second. A schematic overview of the setup can be found in Figure 2.2.

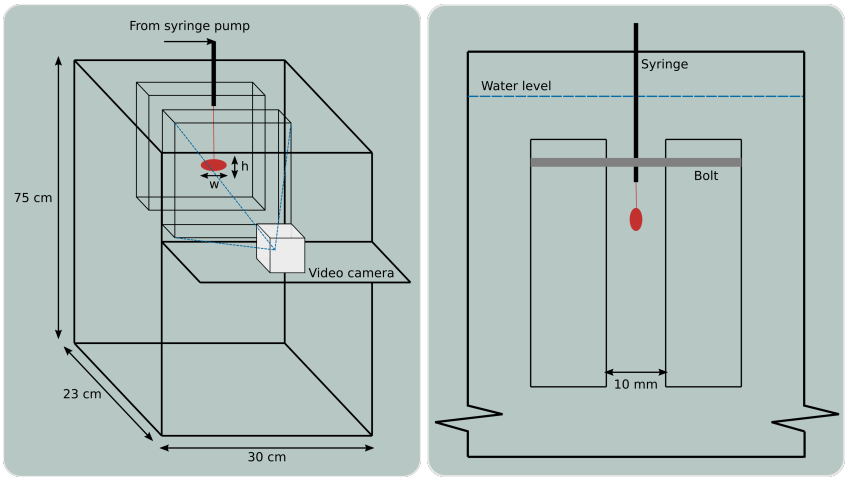

(a) General 3D overview (b) Side view

Figure 2.2: Schematic overview of the experimental setup

2.3. Artificial fractures

Firstly experiments with artificial fractures were performed. This included a smooth fracture and a rough fracture, which are discussed in the following subsections. The macro-model containing an artificial fracture was constructed from at least one acrylic plate, which allowed observation of swarming effects within the macro-model, providing a better understanding and visualisation whether and how swarms affected transport of colloidal particles.

2.3.1. Artificial smooth fracture

The smooth fracture consisted of two smooth, see-through acrylic blocks which are separated by two bolts, as mentioned in section 2.2. Boomsma and Pyrak-Nolte, 2015 found that the ratio of fracture aperture (d) to swarm diameter (w) was an important controlling factor on swarm transport. An optimally confined swarm regime was found for $1 < d/w < 10$, in which swarm bifurcation was inhibited and the swarm was able to move faster and further. It was chosen to perform the experiment with a smooth fracture with $d = 10\,mm$, such that $d/w \approx 5$. This created the most favourable conditions for swarming behaviour to be observed. This fracture aperture was in agreement with the observation that enhanced transport occurred in water for $3.5\,mm < d < 20\,mm$ (Boomsma, 2014).

2.3.2. Artificial rough fracture

Similarly to the smooth fractures, the rough fractured macro-model had a single smooth acrylic block through which the camera could see. The second acrylic block however was replaced by a 3D printed clay fracture. The printed model was attached to the first acrylic block in such a way that the highest peak of the clay fracture touched the acrylic block.

The fracture was based on a 3D scan of a rough clay fracture, created by desiccation of a clay sample obtained from Uithoorn, NL. The clay was wet, but not saturated, when collected and placed in a plastic tub with a diameter of $30\,cm$, where it was left out in the sun to dry for 5 days, with an average day temperature of approximately 20 °C, to let the clay undergo a natural desiccation process.

The wide tub ensured that the boundary conditions of the wall were sufficiently far away to prevent ”U-shaped settling” from occurring, as a result of clay sticking to the wall of the tub (Pengel, 2016). The desiccation process resulted in multiple fractures, with apertures ranging from $1\,mm$ up to $10\,mm$. Images of the clay sample when it was collected from the field and during and after desiccation can be found in Appendix B.

The clay sample broke into 3 large chunks, which were digitized via 3D scanning (EinScan Pro). The digital clay samples had multiple sides, only the sides which were part of a clay-clay fracture were cut off and used for further analyses; the clay sides that got detached from the plastic tub were discarded. In total, 5 clay sides were long enough to combine into a single new, artificial, clay fracture. The fracture sides were laid down side to side, such that the original flow direction (top to bottom though a fracture) was maintained. The bottom of a fracture wall was thus connected to the top of the following fracture wall (see Figure 2.3).

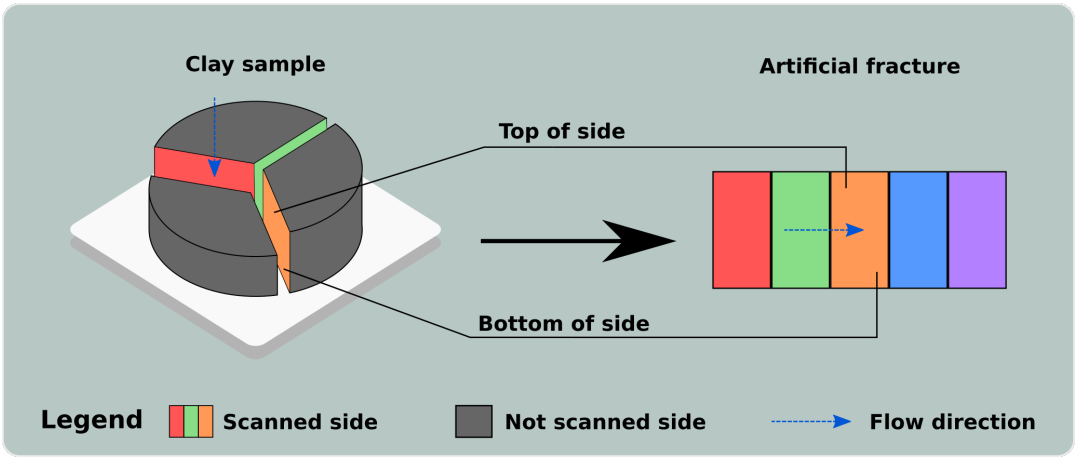

Figure 2.3: Figure illustrating the processing method of turning multiple fracture walls into a new artificial fracture.

The resulting new fracture had large height differences. Since in a real fracture, the walls run semi-parallel to each other, aperture width throughout the fracture does not vary extremely within a single fracture. However, because the artificial fracture was to be matched with a straight, flat acrylic block, this would have been the case for the artificial sample. The new artificial clay sample was therefore rescaled, such that the peaks on the fracture wall were reduced. The peak in the original artificial fracture was $28.6\,mm$, but after a rescaling factor of 0.350, the peak in the rescaled artificial fracture was $10.0\,mm$ (see Figure 2.4). Hence, since the artificial fracture was placed with the highest point touching the see-through acrylic block, the maximum aperture was $10\,mm$. This value matched the largest observed fracture in the original desiccated clay sample. In addition, this aperture, with approximately $0 < d/w < 5$, was most likely within the optimal aperture regime. Finally, the artificial fracture was cropped to a $10\,mm * 10\,mm$ plate. It should be noted that rescaling of the artificial fracture did cause a reduction in surface roughness, as peaks and valleys were smoothed out. However, the artificial rough fracture did provide a significantly different condition from the smooth fracture and was therefore a good step towards increasing complexity of the geometry of the macro-model.

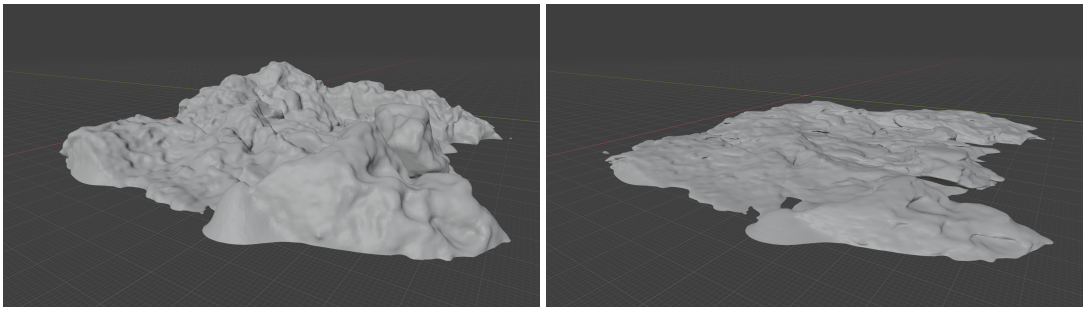

(a) Original unscaled artificial clay fracture. (b) Rescaled artificial clay fracture

Figure 2.4: Artificial clay fracture before and after rescaling with a factor 0.350 in z direction.

Lastly, the clay sample was 3D printed by using a technique called Fused Deposition Modeling (FDM). A thin polylactic acid (PLA) wire of $0.4\ mm$ thickness is pushed through a heated nozzle and builds up the sample in layers. The accuracy of the printing process was $0.1mm$. By printing the artificial fracture wall in a vertical position, the layers of the printing technique were less defined, resulting in a more continuously varying asperity difference, rather than distinct layers.

2.4. Artificial porous medium

The artificial porous medium was based on the pore network of a material called ”highly porous waste ceramics” or ZOAK (TileSystems, NL), as abbreviated in Dutch. The porosity of the sample was determined with the following equation.

$$n = \frac{V_p}{V_t} = \frac{V_t - V_s}{V_t} \tag{2.1}$$

In which n is the porosity $[-]$, V_p is the volume of pores, V_t is the total volume and V_s is the volume of solids, all in $[m^3]$. The ZOAK sample was measured 4 times along each axis and the averages were taken to compute the total volume. Then, the ZOAK was put in a passively ventilated oven and weighed until its mass did not significantly change between days. Then, the sample was put in a tank with a known volume of water and the increase of volume was measured, which is equal to the V_s. The porosity was computed and was equal to 0.228.

To create an artificial pore network, a $1.5\,cm$ thin slice of ZOAK was cut into two parts of $4\,cm * 4\,cm$. These parts were taped together and scanned in a Micro-CT scanner (Phoenix Nanotom Micro-CT scanner), with a resolution of $45\ \mu m$ (also see Appendix C). The resulting dataset was analysed using the *pydicom* package in Python. The ZOAK piece was reconstructed from 861 x-ray photos, or ”slices”, the top- and bottom-most slices were cut off as they did not accurately represent the sample due to scattering. The ZOAK was virtually rebuilt as a matrix with values of the elements between 2714 and 26192, which can be correlated to the Hounsfield scale, a measurement of radiodensity (larger values are more dense). The threshold for identification of a pore was set at 6500, resulting in values below the thresholds being categorized as pores, whereas above this threshold, elements were categorized as solid material. This threshold was determined based on the computed resulting porosity and the measured porosity of the sample, which were matched. Then, the virtual matrix was analysed for a depth of 50 slices, or $2.25\ mm$ of ZOAK, and the pore spaces within this range were summed. Every time a pore was encountered in a slice, it was allowed to overwrite an earlier found solid element, such that the number of pore elements built up. This method created a 2D representation of a 3D network by ”flattening” multiple slices into a single one (see Figure 2.5).

The resulting image contained pore spaces but was not yet a pore *network*, as there were no paths for the colloids to travel through. The image was therefore modified (Sirivithayapakorn and Keller, 2003) such that a pore network was created that connected the top and bottom of the sample. To prevent straining of colloids in the pore network, which is the trapping of particles that are too large to pass through some critical pore space (McDowell-Boyer et al., 1986), pore diameters of approximately $1.5\ mm$ were manually constructed. This value was based on Beven and Germann (1982), who proposed that macropores are in the order of magnitude of $2\ mm$. To enable swarms to move through the pore network, it was necessary to create pores of this size, since straining is an important mechanism for colloids with a diameter of $3\,\mu m$ (Bradford et al., 2004; Bradford et al., 2002) and this process should not hinder the colloidal swarms. Both the original and modified network can be seen in Figure 2.5.

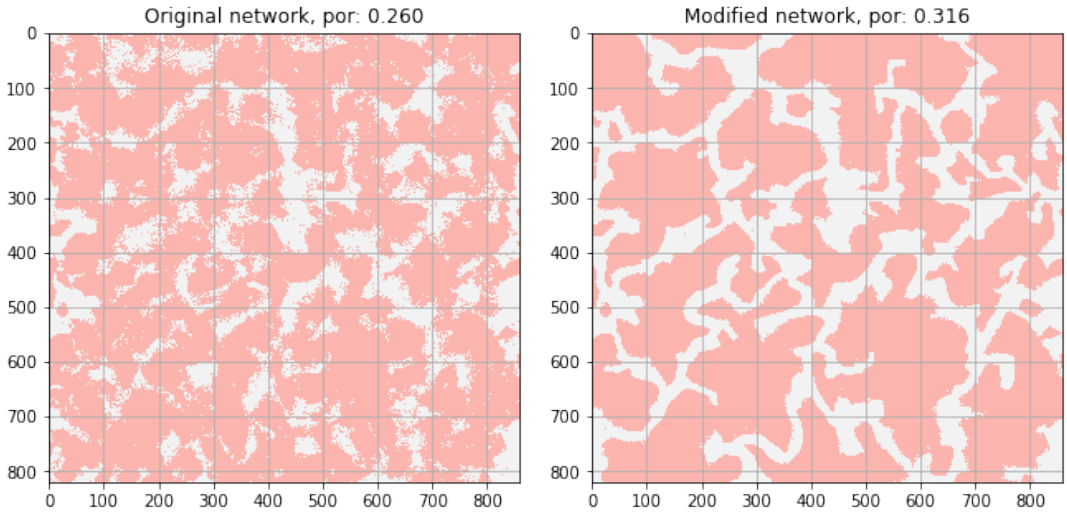

(a) Original pore network

(b) Modified pore network

Figure 2.5: Red represents solid medium, white represents the pore spaces. Values on the axes in pixels

Since the ZOAK sample was approximately $4\ cm\ *\ 4\ cm$ and the macro-model requires a size of $10\ cm\ *\ 10\ cm$, the network had to be upscaled. However, before upscaling was performed, the pores in the network were narrowed, such that they had realistic dimensions in the upscaled version. The pores in the matrix were narrowed based on the adjacent cells; the more ”walls” surrounding the cell of interest, the higher the probability that this cell was converted to a pore wall. This method was applied 4 times to the modified network, such that the porosity of the final network (0.233) closely matched the measured porosity of the real ZOAK sample (0.228). The network was then modified one last time to remove the last bits of noise and upscale the image to $10\ cm\ *\ 10\ cm$ (see Figure 2.6). The tortuosity of the artificial pore network was computed with the following equation.

$$\tau = \frac{L_p}{L} \tag{2.2}$$

Where τ is the tortuosity $[-]$, L_p the length of the travelled path $[m]$ and L the straight distance between the ends $[m]$.

The length of the travelled path was determined with the *A* pathfinding algorithm* in Python (Collingwood, 2021; Swift, 2020) and was performed on a downscaled version of the sample to reduce the computational intensity. The tortuosity was determined in both height and width direction and were 1.484 and 1.480 respectively.

It should be noted that the final pore network as seen in Figure 2.6b was rotated 90 degrees counter-clockwise to ensure a sufficiently wide opening for insertion of the needle in the final pore network geometry (Figure 2.7a).

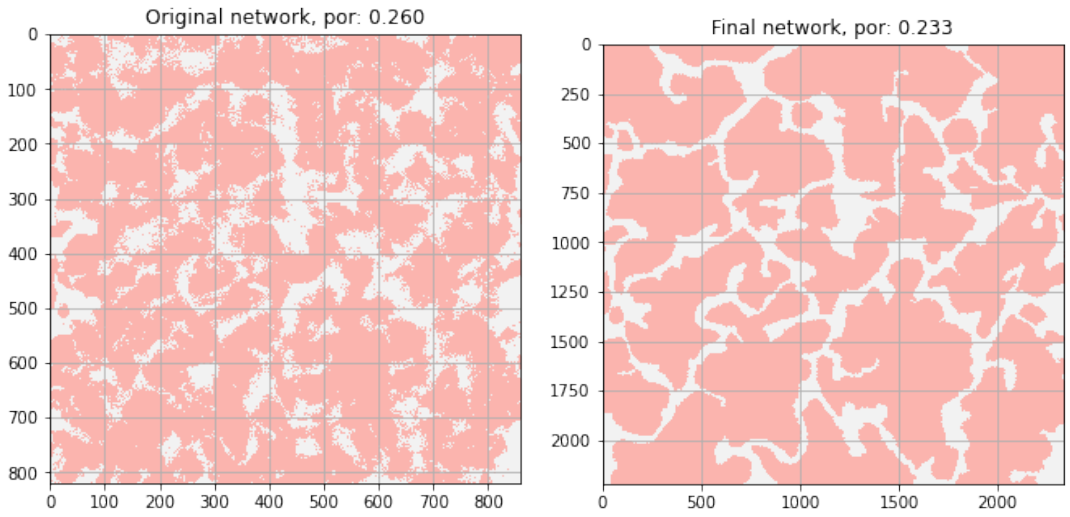

(a) Original pore network

(b) Final pore network

Figure 2.6: Red represents solid medium, white represents the pore spaces. Values on the axes in pixels

Finally, the pore network was 3D printed using FDM. The depth of the pore network was set at $2mm$, whereas the whole plate had a thickness of $4\ mm$. The 3D printing technique resulted in some small sharp points on the plate, which were the ends of the heated PLA wire; these were carefully scraped off with a chisel.

The pore network contained many dead-end channels and a larger cavity close to the point of particle injection, in which the colloidal particles got stuck, reducing the available number of particles that could travel further through the pore network. To investigate the propagation of the injected particles in the confining pore network geometry without losing a significant portion of particles, the pore network was rotated an additional 90 degrees counter-clockwise (Figure 2.7b). This pore throat provided a new geometry to investigate the swarming of particles in.

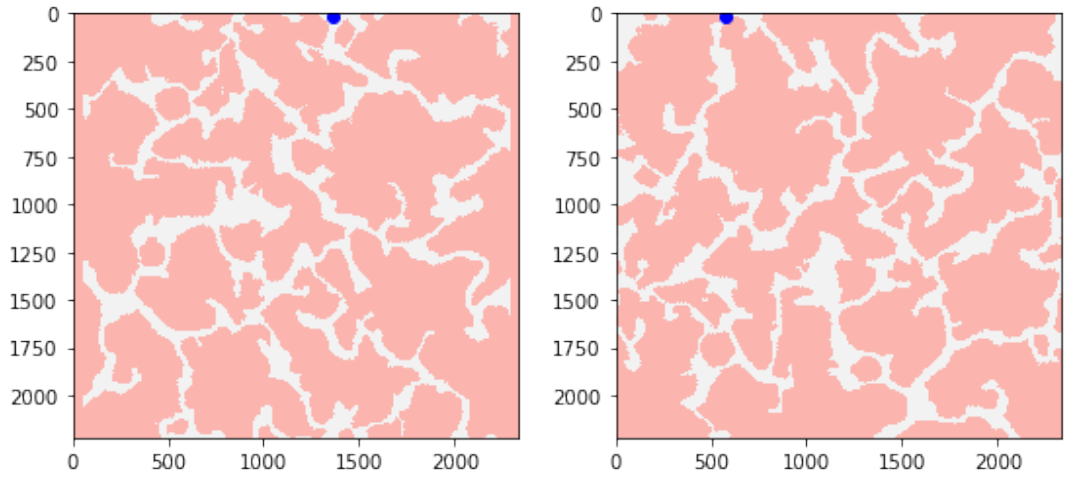

(a) Pore network (pore geometry 1)

(b) Rotated pore network (pore geometry 2)

Figure 2.7: Injection location of colloidal particles (blue point) in the pore network and its rotated version

2.5. Analysis of colloidal swarms

To analyse the behaviour of colloidal particle swarms, firstly the video footage had to be processed (Subsection 2.5.1), which is summarized in Figure 2.8. Secondly, parameters from the video analysis had to be evaluated and selected for usage in the colloidal swarm data analysis (Subsection 2.5.2).

2.5.1. Video footage processing

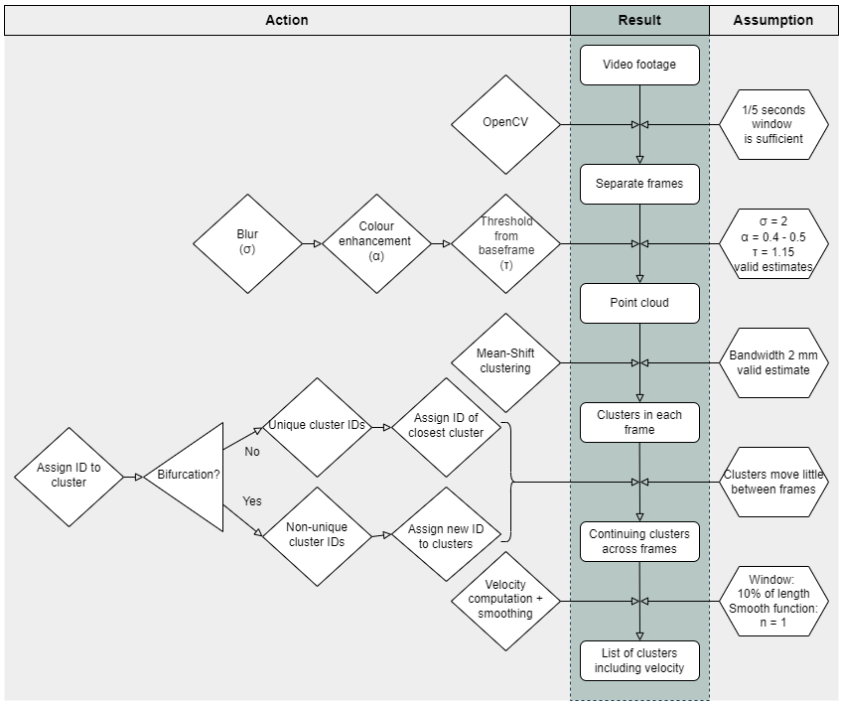

Figure 2.8: Flowchart summarizing the method of processing video footage to obtain clusters along with their parameters.

The camera captured the colloidal particles as they moved through the macro-model. In order to determine relevant parameters, such as swarm dimensions and velocity, custom code was developed in Python.

Firstly, the 25 fps camera footage was converted to separate frames using the *OpenCV* package for Python (Weaver, 2017) (see Figure 2.9a). Due to the relative slow movement of the particles, only each fifth frame was taken, the remaining frames were discarded. The frames were cropped such that the measuring tape for the pixel to millimeter conversion, the sides of the macro-model and the bolts were cropped out of the frame.

Secondly, the frames were slightly blurred with a Gaussian filter ($\sigma = 2$) to ensure that the swarm was seen as a whole, rather than multiple separate elements. The fluorescent colour of the swarm was enhanced by taking the colour channel of the swarm and subtracting α times the remaining two colour channels (see Figure 2.9b). For the smooth and rough fracture, α was set at 0.5, whereas for the pore network, α was set at 0.4. A base frame was selected in which no swarm was visible and the maximum *redness* (or *greenness* for the preparatory experiments) in the frame was used as a threshold for swarm identification. Since the swarms in the smooth and rough fracture experiments left a trail behind, the base frame was selected just after all clusters had passed and as such, only the trail was included in the base frame. Consequently, the trail of the swarm was not identified as a cluster. If the colour value of a pixel in a frame was larger than 1.15 times the maximum of the base frame, it was converted to a point (Figure 2.9c).

This value was found with trial-and-error to best produce clusters with minimal noise. It can clearly be seen that only the cluster was identified and the small trail it left behind was not converted to points, and thus not identified as cluster. Also note that the two air bubbles in the original image were removed by the Gaussian filter and the colour enhancement.

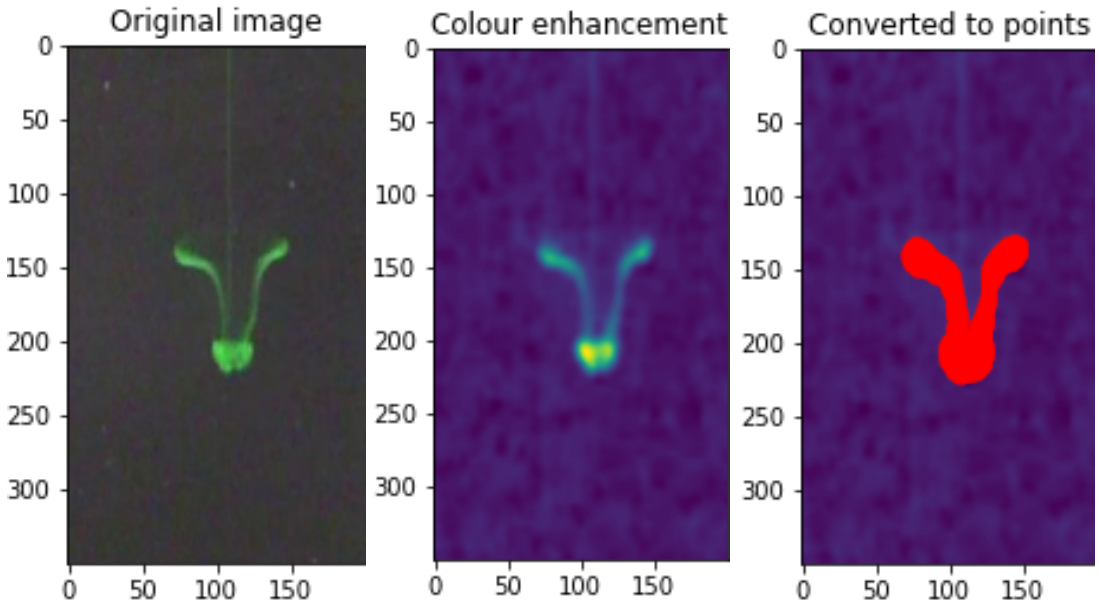

(a) Original camera footage (b) Colour enhanced footage (c) Coloured pixels converted to points

Figure 2.9: Example from the preparatory experiment. Alpha value of 0.4. Values on axes in pixels.

Thirdly, the created points could be used as basis for the *Mean-Shift Clustering Algorithm* in Python (Comaniciu and Meer, 2002; Pedregosa et al., 2011). This machine-learning based algorithm used a sliding-window that searches for the most dense collection of points (Seif, 2018). The algorithm found the center points of each cluster and allowed determination of width and height of each cluster. An advantage of this clustering algorithm was that the number of clusters was not pre-defined. The bandwidth, or window size, had to be defined and determined the region in which the algorithm was allowed to compute the maximum density of points. This bandwidth was optically determined to give good results and was set at $2\,mm$. To prevent noise, such as small bubbles of air, from being identified as clusters, the minimum cluster size was set at $0.5\,mm$. The Mean-Shift algorithm thus identified a cluster and provided their parameters: the x- and z-coordinate of the center (xc and zc respectively). Its width (w) and height (h) could then be computed by using the minimum and maximum x- and z-coordinates respectively. The width and height thus represent the maximum width and height of a cluster.

Fourthly, after clusters were identified along with their parameters, they had to be matched with the clusters from the previous frame. The Mean-Shift algorithm only identified clusters in each frame, but could not relate the clusters between frames. Therefore, the clusters were assigned a unique ID which allowed identification of each cluster. If bifurcation of a cluster did not occur, the clusters in frame `i` could be uniquely related to the clusters in frame `i-1`, based on the distance between them. The clusters in frame `i` were then assigned the ID of the closest clusters in frame `i-1` (see Figure 2.10, left). This technique allowed continuation of a cluster over multiple frames and consequently enabled computation of its velocity (which is elaborated upon in the next paragraph).

However, if bifurcation occurred, the clusters in frame `i` could not be uniquely related to the clusters in frame `i-1`: two clusters would then share the same ID, as two new clusters then both had the same closest cluster (see Figure 2.10, right). The old cluster (frame `i-1`) was then set to inactive, meaning that its ID could no longer be used to relate new clusters (frame `i`) to it. In addition, the clusters in frame `i` that shared a common ID from frame `i-1` were given new IDs and the process repeated. The described method provided a list of clusters with their `xc`, `zc`, `w`, `h`, `ID`, `active` state and `frame` where it was first identified.

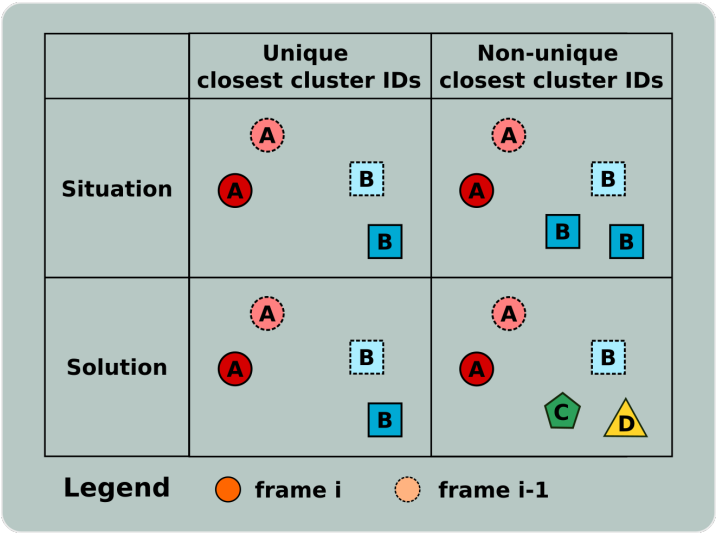

Figure 2.10: Identification of the clusters in frame `i` based on their closest cluster in frame `i-1`. Left shows unique IDs, right shows non-uniqueness of IDs. Each unique cluster is represented by a unique letter, colour and shape

Finally, the velocity (v) of the swarm could be computed. Therefore, the pixels had to be converted to millimeters. A measuring tape attached to the macro-model allowed this conversion. The velocity of a cluster was computed based on the Euclidian distance between the cluster centers between frames.

$$v = \frac{\sqrt{(x_i - x_{i-1})^2 + (z_i - z_{i-1})^2}}{ppm} * \frac{fps}{5} \tag{2.3}$$

In which v is the velocity $[mm/s]$, x_i and z_i the x and z coordinate of the center of the swarm at frame `i` $[p]$, ppm the pixels per mm $[p/mm]$ and fps the frames per second, which was equal to 25. This value was divided by 5, since only every fifth frame was kept for analyses (the time between each analysed frame was thus $1/5\ s$).

In addition, a smoothed velocity was computed (Boomsma and Pyrak-Nolte, 2015), as the velocity showed flashy behaviour. A Savitzky-Golay (backwards) filter (Savitzky and Golay, 1964) was used to smooth position (`xc`, `zc`) data. This filter fitted subsets of data to a polynomial with a user-defined degree via least-squares fitting. The position data was smoothed with such a filter, using a first degree polynomial. Where possible, the window size was set at 10% of the number of frames in which a cluster was active. However, some clusters could only be identified very briefly and were therefore smoothed with a window of 5 frames if 5 ≤frames ≤20, or a window of 3 frames if 3 ≤frames < 5. For clusters that existed shorter than 3 frames, the velocity based on raw position data was directly used. It is important to note that while the smoothed velocity was computed based on the smoothed position data, the used position and size parameters were computed without any filters.

A final remark on the swarm analyses is that the written software in general performed quite well, based on manual comparison with the video footage. There were however cases where clusters seemed to be counted double, i.e. two clusters were largely overlapping, or clusters of only 1 to 3 points long were identified. When overlapping occurred, one of the overlapping clusters was removed, based on which clusters were most poorly visible in the graphs. This mainly occurred in the pore network experiments, due to spreading out of clusters and leaving a large part of their mass behind, which where then identified as new clusters upon bifurcation. Clusters with only few (scattered) points were also discarded, as they were regarded as artefacts picked up or generated by the machine learning algorithm.

2.5.2. Colloidal swarm data analysis

The size and velocity of the swarm give information on how dominant swarm transport was. The particles in a cluster experienced enhanced velocities, since the motion of each sphere was increased due to the motion of the others (Adachi et al., 1978). This *colloidal slipstream* lead to much higher velocities of particles in a swarm than single particles would experience. The velocity of a swarm was therefore a measurement of the dominance of swarming effects. The velocity of the swarm was however highly dependent on the injection velocity (see Appendix D) and the swarm velocity had to be normalised to the injection velocity, which was defined as the velocity of the swarm during the injection period.

The swarm velocity was evaluated at various initial particle concentrations to identify a relationship between these parameters. To fairly compare swarm velocities across the range of concentrations, the average velocity of a cluster before its first bifurcation was used. If a cluster did not bifurcate, this was thus the average velocity over the entire macro-model. Similarly, the average width of a cluster before its first bifurcation was used in the analysis of particle swarming. In addition, the bifurcation process was investigated a bit more closely. For this purpose, the velocity, width and travelled distance up to the point of bifurcation were used.

The above mentioned method however did not hold for the pore network experiments, as the swarms could not settle in an unhindered fashion, since they had to travel through a pore network. The pore walls also provided a confining geometry which guided the swarm and therefore resulted in bifurcation at fixed points; bifurcation parameters such as its velocity and width at bifurcation were therefore not used. Moreover, the injection velocity stagnated directly after injection due to the confining pore network. The average velocity of the swarm in the pore network could therefore not be normalised to the injection velocity.

Since in the pore network clusters did not follow a single path, the average velocity of the swarm was computed based on the furthest travelled distance of a cluster over the time it took for that cluster to reach this point. The ratio of the average velocity of the swarm in the pore network to the average velocity at 0.5% initial particle concentration in the pore network was also evaluated, to enable theoretical analysis as discussed in Chapter 3.

2.6. Validation of experimental setup

To evaluate the effectiveness of the experimental setup, one would usually check the agreement between the series of experiments, which were performed in triplicate. However, since the behaviour of colloidal particle swarms was so chaotic (Machu et al., 2001; Metzger et al., 2007; Myłyk et al., 2011) and experiments in triplicate were not sufficient to obtain and apply rigorous statistics, the experimental setup had to be validated differently. Experimental results were therefore compared to those of Boomsma and Pyrak-Nolte (2015), who used the same particles and a similar setup.

Since the work of Boomsma and Pyrak-Nolte (2015) was focused on varying fracture apertures, much of his presented results were normalised to open tank ($40\ mm$ smooth aperture) experiments. To fairly compare the results to their work, open tank experiments were performed, of which the results can be found in Appendix E. Due to the importance of the open tank results and the large variation in experimental results (Machu et al., 2001; Metzger et al., 2007; Myłyk et al., 2011), these experiments were performed 5 times at each concentration. The results were normalised based on the averages of these 5 experiments. It should be noted that the velocities in the open tank experiments were also normalised first to the injection velocity.

2.7. Assessing the particle leakage rate

In order to study the experimental results with theoretical models (Chapter 3), the number of particles inside a cluster, or *blob* (a spherical cloud of particles), had to be determined. Moreover, since the particle leakage rate may be directly related to the velocity of the falling blob (Nitsche and Batchelor, 1997), it was of importance that the leakage rate was determined based on the available experimental results. Because the particles could not be counted individually due to their size, a method was developed to use the colour intensity as a proxy for the number of particles.

It was known that particles were ejected from the blob at the rear (Machu et al., 2001; Metzger et al., 2007; Myłyk et al., 2011), as a result of the streamline pattern transporting particles that end up just outside of the blob due to random displacements (Nitsche and Batchelor, 1997). Observing the colour intensity of the tail thus provided a method to evaluate particle leakage from the blob.

Another technique to evaluate particle leakage rate was by looking at the colour intensity of the blob (rather than the tail), to assess its number of particles. In both method, data was processed in such a manner that the number of particles in the blob was estimated.

2.7.1. Particle leakage via tail analysis

Firstly, to assess the particle leakage via the tail, it had to be determined which part of a swarm was the cluster and which part was its tail. The clustering algorithm provided the coordinates which belong to the cluster. The top most coordinate, z_{min}, marked the top of the cluster and hence beginning of the tail. Note that $z_{min} = z_{needle} = z_0$ in the first frame. The difference in z_{min} between frame `i` and frame `i+1` provided a window with length Δz, over which the tail could be analysed (Figure 2.11). It was therein assumed that there are little to no particles in this window for frame `i` that fall down such that they are also included in the window in frame `i+1`. The window width was set equal to the width of the blob, since this was wider than the tail and resulted in less computational time due to a smaller window size. Analysed frames were taken 1 or occasionally 2 seconds apart (when velocity was substantially lower) to limit computational time. Analysis started when the injection of particles had finished. The tail analysis was performed up to the point where clusters would bifurcate. After bifurcation, the technique of finding the windows for tail analysis would get significantly more complicated and this is left for a future study.

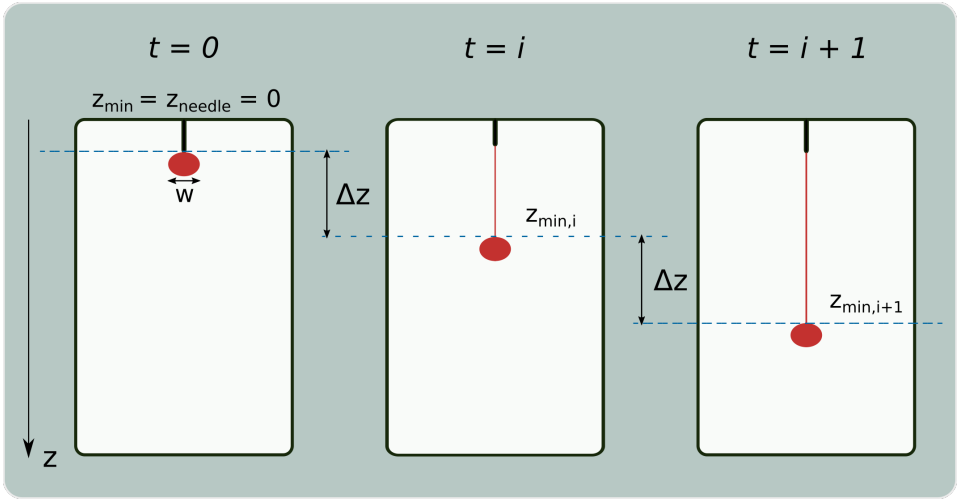

Figure 2.11: Schematic overview of the method to find z_{min} and Δz for the analysis of particles leaking through the tail.

Secondly, the colour intensity of points that were brighter than 1.15 times the baseframe (as explained previously), was summed (see Figure 2.12c). It should be noted that this method is sensitive to selection of a baseframe. With only a one frame difference (1/5 second), the edges of the tail were extended or reduced, leading to an estimate in leakage rate that could differ with $O(10E05)$ particles per analysed frame. Baseframes were optically selected to provide a good boundary of the tail. For this method, it was chosen to use the sum of the colour intensity, as this was able to account for the shape of the tail. An equal number of particles spread out over a wider tail would result in more points to sum, but lower colour intensity per point. Conversely, a thin and concentrated tail would have only few points, but the colour intensity of these points would be large.

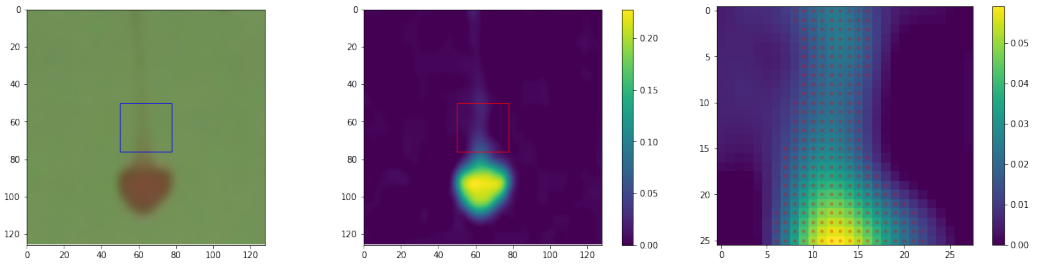

(a) Original camera footage, blue box indicates window in which tail is analysed

(b) Colour enhanced footage, red box indicates window in which tail is analysed

(c) Zoomed in tail. Points marked red pass the threshold

Figure 2.12: Example of determining the window for the tail and computing the colour intensity

Lastly, the sum of the colour intensity had to be related to a number of particles present in the tail. The relationship between number of particles and sum of colour intensity could be found by investigating the first frame right after injection had ended. In theory, all particles should then have been injected and the number of particles was thus known. This can then be related to the sum of the colour intensity of the swarm (see Appendix F). For each series of experiments, a new trend line was computed, since slight changes in lighting conditions that may have occurred affected the colour intensity measurement.

2.7.2. Particle leakage via blob analysis

To limit susceptibility of the leakage analysis to selection of the baseframe, a second method was constructed to evaluate the particle leakage from the swarm, not by estimating the number of particles leaving the tail, but rather by assessing how many particles remained in the cluster. The uncertainty of the baseframe selection was eliminated by only taking a circle in the center of the blob. The center of the blob had a large enough colour intensity to pass the threshold, even with variation in the baseframe.

Firstly, the center of the blob was found with the Mean-Shift clustering algorithm, as elaborated upon in Subsection 2.5.1. Both a circle with a varying radius of $0.2 * R_{blob,min}$ and with a fixed radius of $7.5\ pixels$ were set up with the center of the blob as center of the circle. These dimensions were chosen such that these circles would only include the blob and did not cover the area outside of the blob. A varying radius was used since this allowed investigation of the core of the swarm only. As the width and height of the blob changed, the circle in which the colour intensity was evaluated varied along, as this circle was 20% of the smallest dimension (width or height). However, this would mean that the colour intensity was not always taken over an equally large area. This is why a fixed radius was also used to assess the number of particles in the blob.

Similar to the tail analysis method, the colour intensity of points in the circle was computed. However, the blob analysis used the average of the colour intensity, to limit the effect of the size of the circle. The average colour intensity could then be related to the number of particles by looking at the average colour intensity in the circle just after injection at all concentrations, for both the varying radius and the fixed radius (Appendix F).

2.7.3. Particle leakage in the pore network

When attempting to estimate the particle leakage in the pore network, it became clear that both the tail and blob analysis method were not suitable for assessing the particle leakage rate in the pore network. Many clusters were identified each frame, rendering the above described methods too complicated to use.

Therefore, a new method was devised in which subsequent frames were subtracted from one another (Figure 2.13), such that the travelled distance between frames was highlighted. The parts of the swarm that were present in the new frame got a high colour intensity, since the swarm was not present at those locations in the previous frame and the subtracted colour value was thus low. Having found the travelled distance of the cluster between frames, it was assumed that all particles above the travelling part remained in the pore network and their colour intensity (based on the reference to the baseframe) was summed. This value was then a proxy for the cumulative number of particles 'trapped' in the pore network and as such was a measure for the particle leakage rate from the swarm.

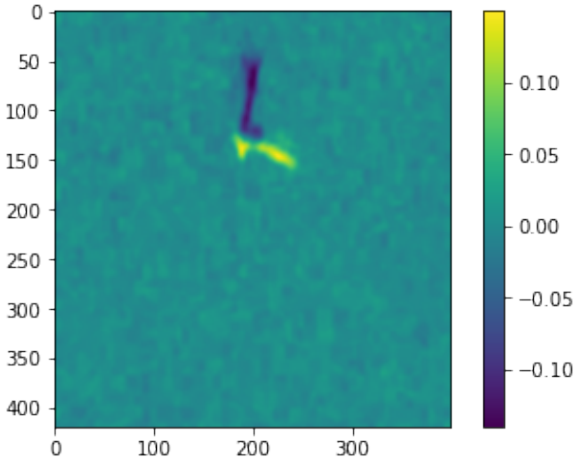

Figure 2.13: Example of subtraction of 2 frames. Bright green indicates high colour intensity, dark blue a low colour intensity. Values on axis in pixels

2.8. Preparatory experiments

Before the experiments with the fluorescent polystyrene beads were performed, preparatory experiments were done with the setup as described in Section 2.2 and 2.5, to verify the existence of an optimal confinement range as suggested by Boomsma and Pyrak-Nolte (2015). In addtion, these experiments allowed optimization of the experimental setup and analyses method before the experiments with colloidal particles were performed.

These preparatory experiments were performed with a uranine solution ($0.112 g/L$) to which salt was added ($51.19 g/L$), in order to set the density of the solution to $1.051 g/cm^3$. This solution resembled the density of the colloidal particles used in the experiments ($1.05 g/cm^3$). The added salt created a density flux, which ensured a downwards motion of the solution and hence, a better imitation of the behaviour of colloidal particles. The added uranine gave the solution a bright green colour which allowed tracing of the clusters as they moved through the macro-model. The uranine solution was injected only into the smooth fractured macro-model with fracture aperture set at $4\ mm$, $10\ mm$ and $16\ mm$. With each experiment, $25\ \mu L$ was injected at a rate of $5\ mL/min$ and the resulting cluster formation was analysed as discussed previously. It should be noted that the colour enhancement was performed in the green channel, with a subtraction of $\alpha = 0.4$ times the red and blue channel. The results of the preparatory experiments can be found in Appendix G.

To investigate the role of temperature in the experiments, the water temperature was closely monitored during a full series of experiments. Two divers were used, located at the top and bottom of the tank (Appendix H. Measurements showed only a 0.1 °C difference between the top and bottom of the tank and increments in temperature of the same order of magnitude. Increase in water temperature during an experimental series and temperature gradient induced flow was therefore assumed negligible.

The large variation in injection velocity gave rise to the question whether the used syringe pump was accurate in its ejected volume. The accuracy of the pump was therefore tested in triplicate (each with a new syringe), measuring each ejected volume 5 times on an analytical balance (Mettler AT261) at 5 different volumes (Appendix H). The standard deviation of ejected volume was low, at $0.24\ \mu L$. It was assumed that this standard deviation could be ignored compared to the effect of the injection velocity of the pump and did not cause the observed difference in velocities between series of experiments.

3

Modelling of Colloidal Swarms

There are multiple authors that have numerically modelled suspension drops falling under gravity (Machu et al., 2001; Metzger et al., 2007; Myłyk et al., 2011). The modelling in this thesis was done for interpretation of the results, rather than prediction of experimental data. Simple models were used to investigate the effect of concentration on the velocity of a cluster, in smooth and rough fractures and in the pore network. This chapter will firstly discuss the first order modelling of the velocity of particle swarms in fractures, after which the pore network is discussed.

3.1. Modelling particle swarm movement through a smooth and rough fracture

A simple analytical equation for the velocity of a falling cluster of particles was presented by Nitsche and Batchelor (1997). The analytical equation approximates their numerical model well and was thus promising.

$$\frac{V_b}{v_0} \approx \frac{6}{5} N_b \epsilon + 1 \tag{3.1}$$

In which V_b is the velocity of the blob $[m/s]$, v_0 the single particle settling velocity $[m/s]$, N_b the number of particles in the blob and ϵ the ratio of particle radius (a $[m]$) over swarm radius (R $[m]$). It should be noted that the hindered settling effect was ignored (Nitsche and Batchelor, 1997). The last term in Equation 3.1 was required, as a correction needs to be made for existing slip conditions. However, when $N >> R/a$, the slip becomes irrelevant and the last term could be ignored; for all concentrations used in the experiments in this thesis that was the case. The resulting equation was similar to the analytical equation in the work of Chassagne (2019), who presented the solution of Hadamard (1911) and Rybczynski (1911) for a falling fluid drop in a lighter medium.

$$V_s = N_b \frac{6a}{2\frac{2+3\lambda}{\lambda+1}R} v_0 \tag{3.2}$$

In which V_s is the terminal velocity of a spherical swarm of particles $[m/s]$ and λ is the ratio between the cloud viscosity and the viscosity of the fluid medium.

For a dilute swarm of particles, $\lambda \approx 1$ and the term $2\frac{2+3\lambda}{\lambda+1}$ becomes 5. Equation 3.1 and 3.2 then give identical results. However, since Equation 3.2 provided more freedom in selecting λ, it was chosen to use this equation to investigate the effect of concentration on the velocity of particle swarms in smooth and rough fractures.

The parameters in the Hadamard & Rybczynski (HR) equation (Eq. 3.2) were taken from the swarm and particle leakage analysis, with the exception of λ, which can be used as a fitting parameter via a non-linear least squares fitting function. The model results were then compared to the data, resulting from swarm analysis, and mismatch to the data could be explained by using the HR formula.

3.2. Modelling particle swarm movement through a pore network

The smooth and rough fracture experiments were both examples of a gravity driven settling cluster of particles, also called a blob. In the pore network however, there were no free falling conditions, since the pore walls confined the particles to its geometry. The equations used in the fracture did thus not hold for the pore network.

However, the pore network could be seen as a system of tubes under various inclinations. An interesting phenomenon that occurs in such systems is the *Boycott effect*. As the colloidal particles sediment onto the pore wall, a thin sediment layer is formed (C, Figure 3.1), which rapidly moves downward under the effect of gravity and consequently enhancing the settling rate (Chassagne, 2019). Due to the incompressibility of the suspension and the conservation of volume, a clear-fluid moves to the top of the pore throat along the downward-facing pore wall (D, Figure 3.1). An analytical solution for monodispersed particles and negligibly small particle Reynolds number was given by Davis and Acrivos (1985), who stated that, apart from pore geometry and solids concentration, the settling rate was governed by two (dimensionless) parameters. The first one was the sedimentation Reynolds number, Re_s and the second one was the ratio of the sedimentation Grashof number to Re_s, Λ.

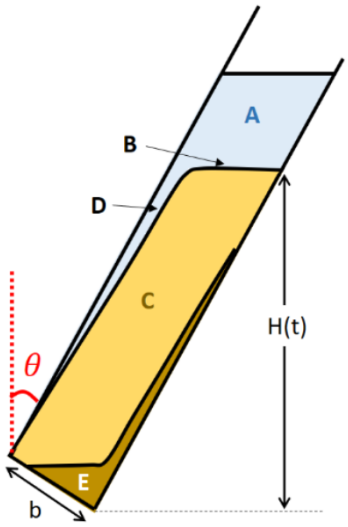

Figure 3.1: Schematic representation of particles sedimenting in a tube. Figure taken from Chassagne (2019)

$$Re_s = \rho_f H v_0 / \mu \tag{3.3}$$

With Re_s being the sedimentation Reynolds number, ρ_f the fluid density $[kg/m^3]$, H the vertical height of the suspension $[m]$, v_0 the single particle settling velocity $[m/s]$ and μ the dynamic viscosity $[kg/(m*s)]$.

From this, it followed that:

$$\Lambda = \frac{H^2 g(\rho_p - \rho_f)\phi_0}{v_0 \mu} \tag{3.4}$$

With ρ_s the density of particles [$kg/m3$] and ϕ_0 the volume fraction of particles. Finally, the equation of the clear-fluid layer thickness was required for the computation of velocity through the pore.

$$\delta(x) = \Lambda^{-1/3}(3xtan\theta)^{1/3} \tag{3.5}$$

Where δ is the clear-fluid layer thickness [m], x the x coordinate along the channel wall [m] and θ the inclination of the channel. The equation for the velocity as presented by Davis and Acrivos (1985) was then:

$$u_x = \Lambda^{1/3}(\tilde{y}\tilde{\delta} - \frac{1}{2}\tilde{y}^2)cos\theta \tag{3.6}$$

In which u_x is the velocity parallel to the downward-facing wall of the channel [m/s], $\tilde{y}$ [m] is given by $\tilde{y} = \Lambda^{1/3}y$, with y the distance from the wall [m], $\tilde{\delta}$ [m] given by $\tilde{\delta} = \Lambda^{1/3}\delta$.

Using Equation 3.6, the relationship between concentration and velocity through the pore was investigated. By only varying the particle (volume) concentration, ϕ_0, in Equation 3.4, its effect on the velocity could be determined. It should be noted that Equation 3.6 was not used to compute the exact velocity in the pore network, but only to analyse the value resulting from this equation to compute the ratio of $u_x(\phi = \phi_{0,i})$ to $u_x(\phi = \phi_{0,j})$, in which i is a volume concentration related to either 0.5, 1, 2, 3.5 or 5% concentration by mass and j is the volume concentration related to 0.5% concentration by mass. Thereby, a relationship between concentration and velocity could be inferred. This was done since the pore network consisted of multiple inclined pores and analysis would become too extensive if each pore had to be analysed.

4

Results and Discussion

In this chapter, the results of the experiments are discussed. Firstly, results of the smooth fractures, rough fracture and pore network experiments are presented, after which they are discussed. Secondly, results of the particle leakage analysis are put forward. Finally, the modelling results of the smooth and rough fracture and pore network are presented and elaborated upon. Results of the preparatory experiments can be found in Appendix G.

4.1. Experimental results

This section discusses the results from the injection experiments in the various macro-models. Since observed velocities were highly correlated with the injection velocity, all velocities presented were normalised to the injection velocity of that experiment.

4.1.1. Smooth fracture

Result of validation test

Figure 4.1 shows the velocity of the swarm at bifurcation, at $30\,mm$ and at $60\,mm$ depth. The velocities were divided by its open tank equivalents. Figure 4.2 shows the travelled distance of the swarm to bifurcation over the corresponding open tank value. Results were in line with the results of Boomsma and Pyrak-Nolte (2015) (their Figure 5.8a and 5.8b respectively), successfully validating the experimental setup.

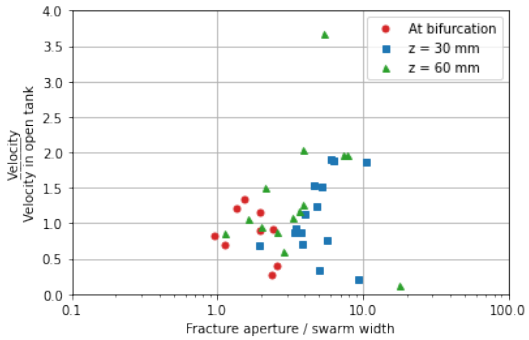

Figure 4.1: Smooth fracture, fracture aperture over swarm width versus the velocity at various depths over their corresponding open tank value

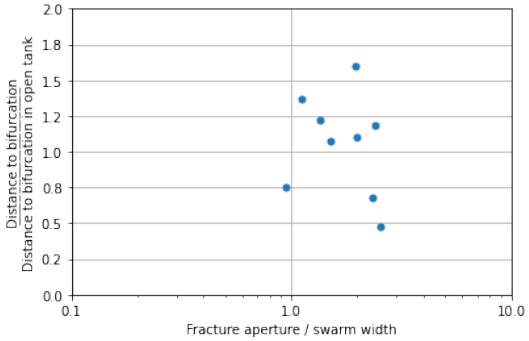

Figure 4.2: Smooth fracture, fracture aperture over swarm width versus the distance to bifurcation over its corresponding open tank value

The found velocities were generally a bit lower, which was explained by a larger open tank velocity, roughly 2-3 times as large. This may be caused by the fact that the injection rate in the experiments of this thesis was twice as large as that of Boomsma and Pyrak-Nolte (2015). In general however, the found results matched well in their order of magnitude.

Velocity of a swarm

The effect of concentration on the average velocity of the cluster until its first bifurcation and its average width are shown in Figure 4.4 and Figure 4.3 respectively.

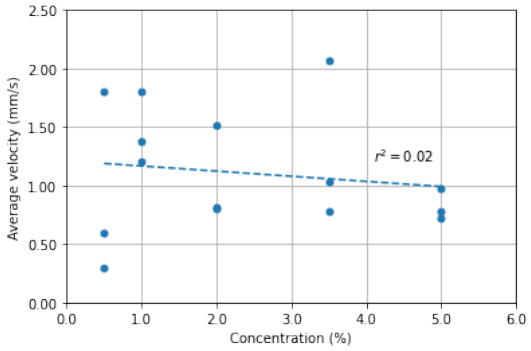

Figure 4.3: Smooth fracture, concentration versus average velocity

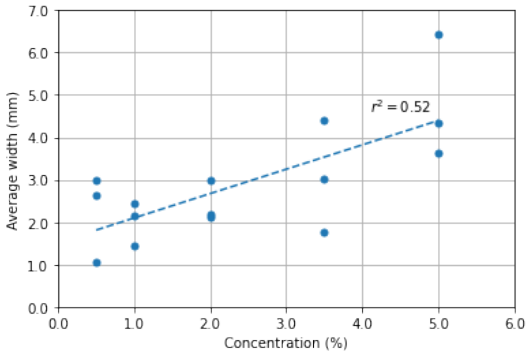

Figure 4.4: Smooth fracture, concentration versus average width

No clear trend could be observed, but a slight declining line seemed to be present. Interestingly enough, the velocity did not increase with concentration, despite the larger number of particles which could have increased the density of the swarm and therefore also increase its velocity.

An explanation can be found by looking at the average width of the cluster until first bifurcation occurred as function of the concentration (Figure 4.4), which clearly showed an increasing average width as the initial particle concentration increased. Although a swarm consisted of many particles, the swarm could be regarded as a single entity that experienced hydrodynamic forces. As with a single particle, the swarm should have experienced larger drag forces as the width of the swarm increased. So, if the width increased, the velocity should have decreased as a consequence and this may explain the slight declining velocity with increasing concentration.

It was indeed the case that the velocity of the swarm decreased as its width increased (Figure 4.5).

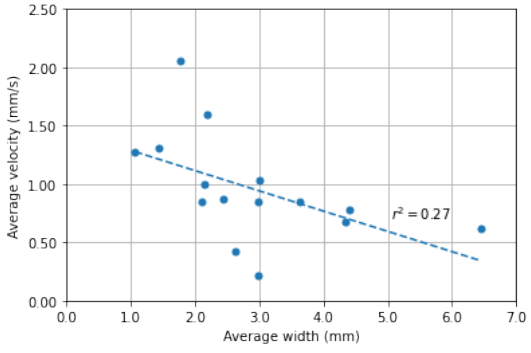

Figure 4.5: Smooth fracture, average width versus average velocity

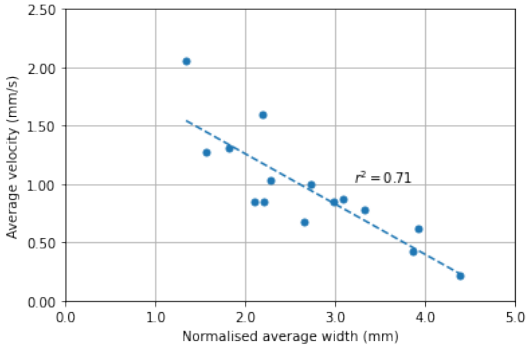

Figure 4.6: Smooth fracture, normalised average width versus average velocity

However, as showed previously, the width was also concentration dependent. When analysing the relationship between width and velocity, the width should be normalised to the concentration in order to separate the effect of concentration and width on the velocity. Having normalised the width to $c_0 = 2\%$ (Figure 4.6), the relationship became even more pronounced: the wider the cluster became, the lower its velocity. This observation matched that of others such as Metzger et al. (2007), who also stated that the flattening of a suspension drop may contribute to the decrease in its velocity.

Bifurcation of a swarm

An intriguing feature of colloidal particle swarms was their bifurcation (Figure 4.7).

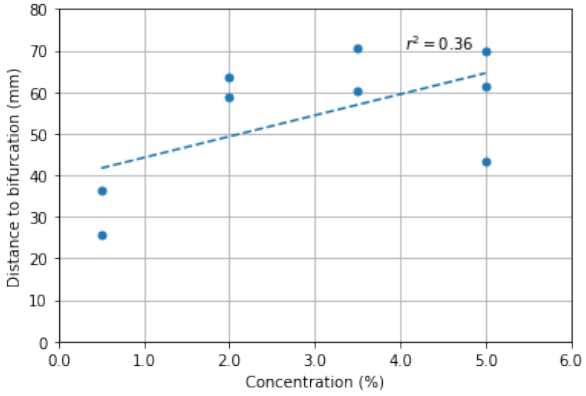

Figure 4.7: Smooth fracture, concentration versus distance to bifurcation

It seemed there was a weak trend that the distance to bifurcation increased with increasing particle concentration, implying that larger initial particle concentrations lead to more stable swarms.

Investigating the relationship between velocity at bifurcation and distance to bifurcation (Figure 4.8) clarified two things: (i) bifurcation did not occur at a threshold velocity below or above which the swarm bifurcated and (ii) the bifurcation distance increased with larger average velocity, since it was highly correlated to the velocity at bifurcation (Figure 4.9). This result was also found in literature, where a larger swarm velocity lead to further travelled distance until break-up (Myłyk et al., 2011).

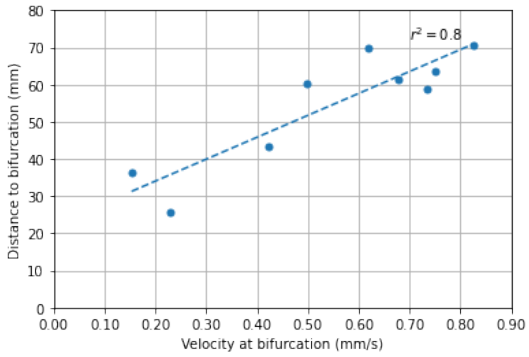

Figure 4.8: Smooth fracture, velocity at bifurcation versus distance to bifurcation

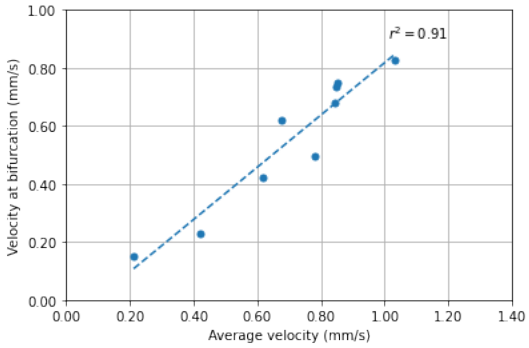

Figure 4.9: Smooth fracture, average velocity versus the velocity at bifurcation

Evaluating the width of the swarm at bifurcation as function of the initial particle concentration also provided new insights.

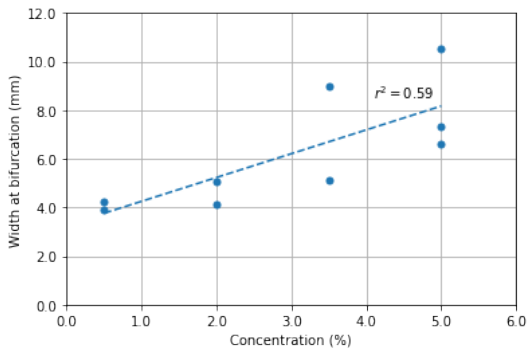

Figure 4.10: Smooth fracture, concentration versus width at bifurcation

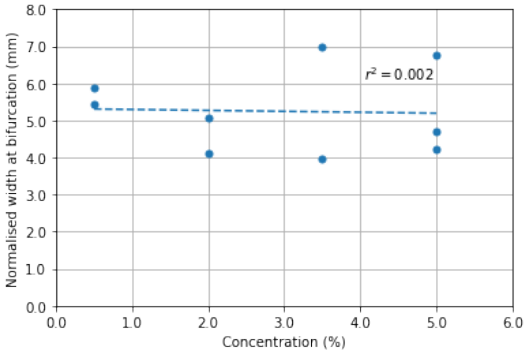

Figure 4.11: Smooth fracture, concentration versus width at bifurcation normalised to $c_0 = 2\%$

The width of the swarm at bifurcation increased with a larger initial particle concentration (Figure 4.10). However, normalizing to 2% concentration (Figure 4.11), it can be seen that bifurcation occurred at a threshold cluster width, just above $5\ mm$. Bifurcation of a cluster thus occurred at a threshold cluster width that linearly increased with particle concentration.

Metzger et al., 2007 reported that break-up of drops occurred at a fixed aspect ratio (which differed between experimental and numerical results). This could not be reproduced in experiments of this thesis. An explanation can be found in the used clustering algorithm used to analyse the swarms. Large heights of swarms were occasionally found due to a *late bifurcation acknowledgement*. At these points, the swarms were already bifurcating if evaluated by eye, visible by the reverse V shape. The algorithm however still identified this V shaped swarm as a single cluster. Only when the arms of the V disconnected, the swarm was acknowledged to have bifurcated and two smaller clusters were identified. This lead to large heights at bifurcation. These differing heights at bifurcation resulted in varying aspect ratios, which may explain why no threshold aspect ratio was found.

In addition, the shape of the injected swarm can greatly affect torus formation and bifurcation (Stone, 1994). Nitsche and Batchelor (1997) reported that their initially shaped cloud was highly stable and maintained its cohesion and size and bifurcation was not mentioned. Metzger et al. (2007) however reported that, although their swarms were spherically shaped, break-up of swarms still occurred. These differences may be explained by the high sensitivity of streamlines to the configuration of the swarm and evolving torus, leading to large variation between experiments (Machu et al., 2001).

4.1.2. Rough fracture

Result of validation test

Both the velocity of the swarm at various depths over their open tank values (Figure 4.12) and the distance the swarm travelled to bifurcation over its open tank value (Figure 4.13) matched the results of Boomsma and Pyrak-Nolte (2015) (their Figures 5.20a and 5.20b respectively). This provided strong evidence that the experimental setup had been correctly implemented.

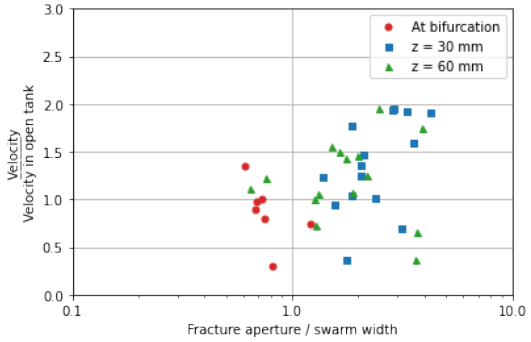

Figure 4.12: Rough fracture, fracture aperture over swarm width versus the velocity at various depths over their corresponding open tank value

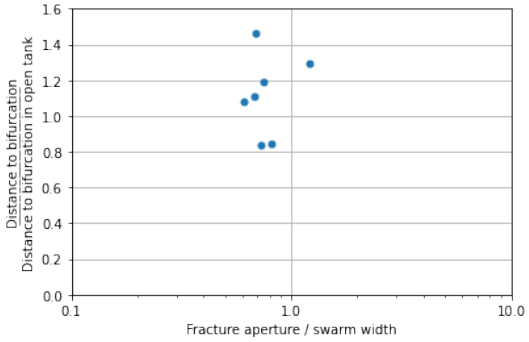

Figure 4.13: Rough fracture, fracture aperture over swarm width versus the distance to bifurcation over its corresponding open tank value

There was less agreement between these experiments and work of Boomsma and Pyrak-Nolte (2015) for the rough fractures than for the smooth fractures, but this was to be expected. The rough fracture in this work differed from their work and inevitably lead to different results. The velocity differed by a factor 3 to 4, which was partially explicable by the larger used injection velocity and may also be attributed to larger height differences in the rough fracture of this thesis, leading to a larger roughness and consequently imposing more drag on the swarm, reducing its velocity. However, results were still generally in the same order of magnitude and the experimental setup was therefore deemed successful.

Velocity of a swarm

The relationship of particle concentration versus the velocity of the swarm and versus the width of the swarm in the rough fracture is presented below.

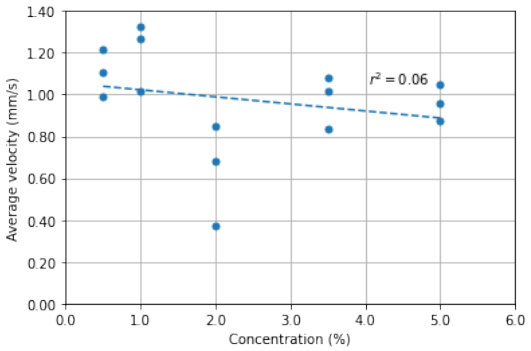

Figure 4.14: Rough fracture, concentration versus average velocity

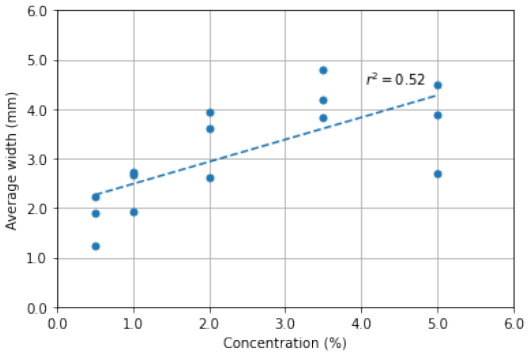

Figure 4.15: Rough fracture, concentration versus average width

The average velocity up to bifurcation did not show a clear relationship, but a slight declining velocity with increasing initial particle concentration hinted toward a somewhat declining trend (Figure 4.14).

Similarly to the smooth fracture, the average width of the swarm until bifurcation occurred increased with larger particle concentrations (Figure 4.15). As discussed before, this larger width lead to a reduction in velocity due to increased drag forces that were imposed on the swarm.

Again, as predicted, the average velocity up to bifurcation decreased as the average width of the cluster increased (Figure 4.16). However, since the width was concentration dependent, normalization of the width to $c_0 = 2\%$ was performed (Figure 4.17) to eliminate the effect of concentration. The declining cluster velocity with increasing cluster width supported the slight trend of declining velocity with increasing concentration (Figure 4.14).

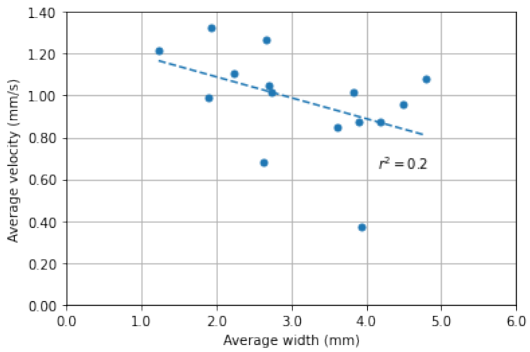

Figure 4.16: Rough fracture, average width versus average velocity

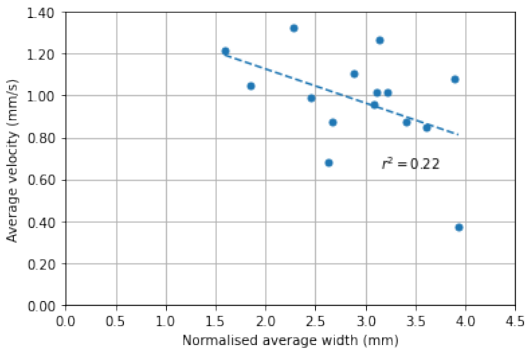

Figure 4.17: Rough fracture, normalised average width (to $c_0 = 2\%$) versus average velocity

The relationship between average cluster velocity and its width was less pronounced for the rough fracture than for the smooth fracture, which may be caused by the additional drag forces imposed on the cluster due to increased roughness of the wall. These asperity differences in the rough fracture may have torn the swarm apart and caused more variation in width, resulting in a poorer linear relationship.

Remarkable was the similarity between the velocity and width of the swarm in the smooth (Figure 4.6) and rough (Figure 4.17) fracture. An explanation may be found in the aperture range of the rough fracture. Boomsma and Pyrak-Nolte (2015) reported that swarms no longer strongly responded to the fracture aperity height for $2.5 < d/w < 5$, but instead showed behaviour similar to that in the smooth fracture. Since the fracture spacing (d) was set at the maximum asperity height of $10\ mm$, the average fracture spacing was less than $10\ mm$ and consequently the d/w ratio may have been too small, causing the velocity and width of the swarm to be more similar in the smooth and rough fracture.

Bifurcation of a swarm

The distance to bifurcation of a cluster seemed to be rather independent of the initial particle concentration (Figure 4.18).

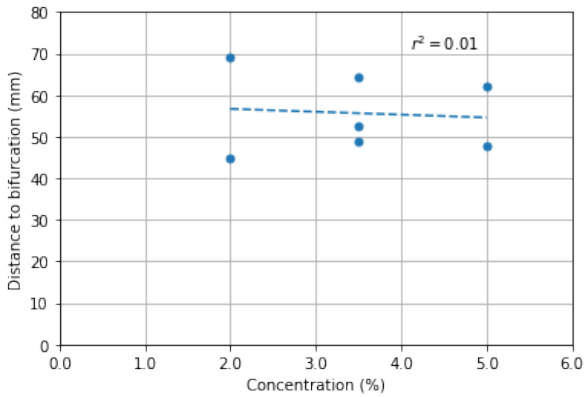

Figure 4.18: Rough fracture, concentration versus distance to bifurcation

Interestingly, clusters appeared to be less prone to bifurcation at lower initial particle concentrations, a finding also reported in work of Metzger et al. (2007).

It could however again be verified that the travelled distance of the swarm to bifurcation depended on its velocity at bifurcation (Figure 4.19), which was correlated to the average velocity up to bifurcation (Figure 4.20).

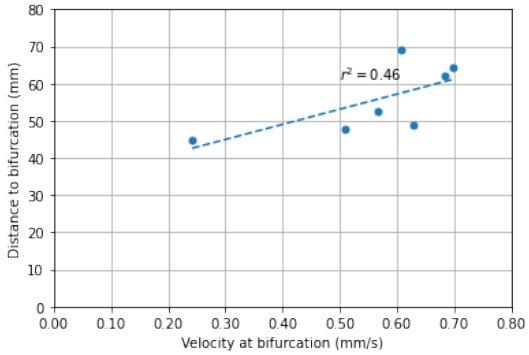

Figure 4.19: Rough fracture, velocity at bifurcation versus distance to bifurcation

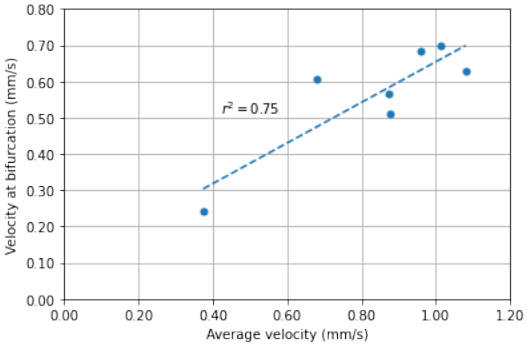

Figure 4.20: Rough fracture, average velocity versus the velocity at bifurcation

Hence, the faster the cluster moved, the further it got before it bifurcated; this matched results found in the smooth fracture. Moreover, like in the smooth fracture, the distance to bifurcation did not occur at a threshold cluster velocity.

The effect of concentration on the width at bifurcation provided valuable insights.

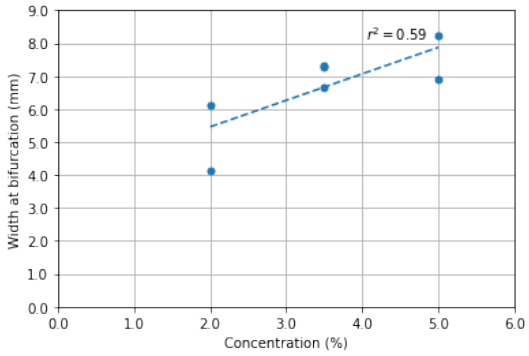

Figure 4.21: Rough fracture, concentration versus width at bifurcation

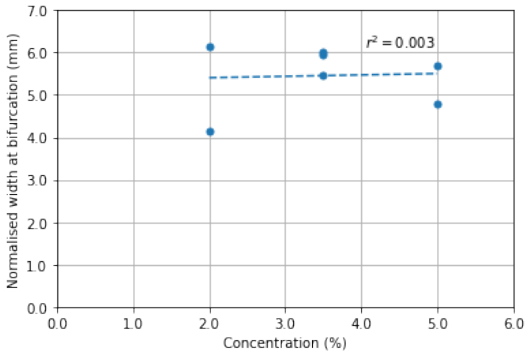

Figure 4.22: Rough fracture, concentration versus width (normalised to $c_0 = 2\%$) at bifurcation

Bifurcation did occur at a threshold cluster width, which can be seen from the normalized (to $c_0 = 2\%$) width at bifurcation (Figure 4.22). This threshold matched the $5.2\,mm$ found in the smooth fracture. Moreover, the same relation between swarm width at bifurcation and particle concentration (Figure 4.21) was found for both the rough and smooth fracture. This could either indicate that the bifurcation width threshold was unaffected by the confining geometry, or reaffirmed the hypothesis that the fracture walls may have been placed too close together, which lead to similar behaviour in the smooth and rough fracture. It was most likely the former, since the normalised cluster width at bifurcation in the open tank experiments (Figure 4.23) also showed a threshold width of $5.5\ mm$ at a particle concentration of 2%.

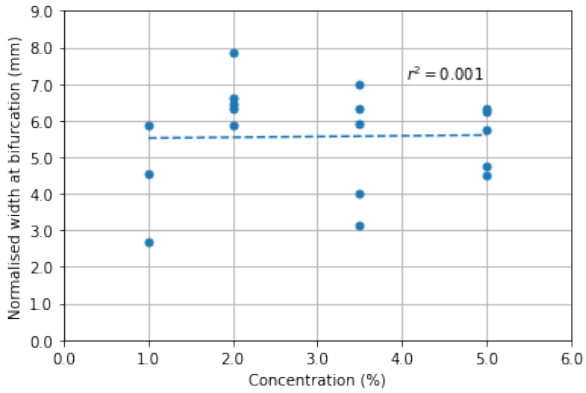

Figure 4.23: Open tank, concentration versus the the width (normalised to $c_0 = 2\%$) at bifurcation

4.1.3. Pore network

The average velocity in the pore network followed a strong linear increase with increasing concentration (Figure 4.24) for both sets of experiments in pore geometry 1, as well as pore geometry 2.

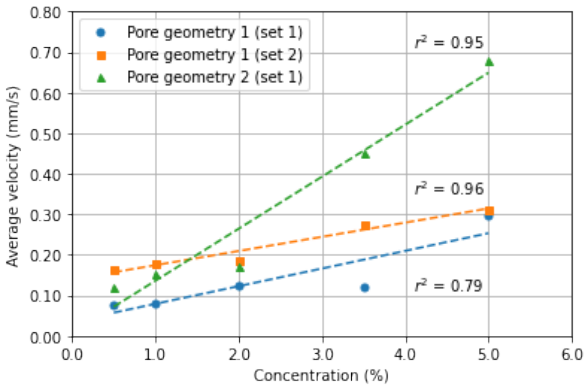

Figure 4.24: Pore network, concentration versus the average velocity

At higher concentrations, pore geometry 2 showed a larger average swam velocity than the pore geometry 1. At all concentrations, the swarm flowed through the pore network as a viscous fluid, resembling the flow of lava down a volcano. Interestingly so, the travelled distance did not differ significantly at various concentrations (Figures 4.25a & 4.25b), meaning that the increase in average velocity was solely due to faster (average) movement of the swarm through the network. The larger observed velocity at higher concentrations could be caused by the increased number of particles in the swarm, resulting in larger mass and thus larger gravitational driving force. This, in combination with a lack of swarm widening with increasing particle concentration, may have lead to an increased velocity with increasing concentration.

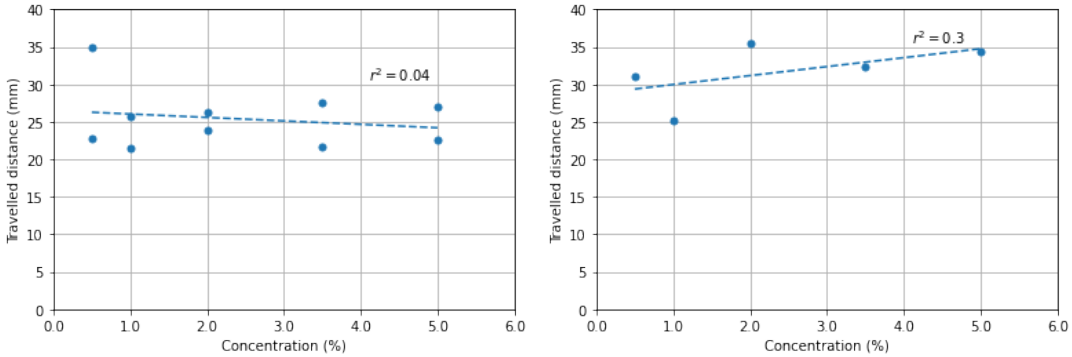

(a) Pore geometry 1 (b) Pore geometry 2

Figure 4.25: Pore network, concentration versus travelled distance in the original and rotated pore network

After injection, the swarm shortly came to a halt due to the confining geometry of the pore network, after which it quickly settled to the upward facing pore wall. The swarm was guided through the pore network by the pore walls. Upon an encounter with a cavity in the pore wall, the swarm followed the *fill and spill* theory. The particles would fill up a cavity and, once full, spilled over, after which the particles continued their way down the pore wall.

When the upward facing pore wall ended, the particle swarm initially fell straight down at the edge of the upward facing wall, creating a waterfall of particles (Figure 4.26a). Shortly after however, particles seemed to follow the pore wall a bit longer, sticking to the wall after which they eventually detached and continued their way downwards too (Figure 4.26b).

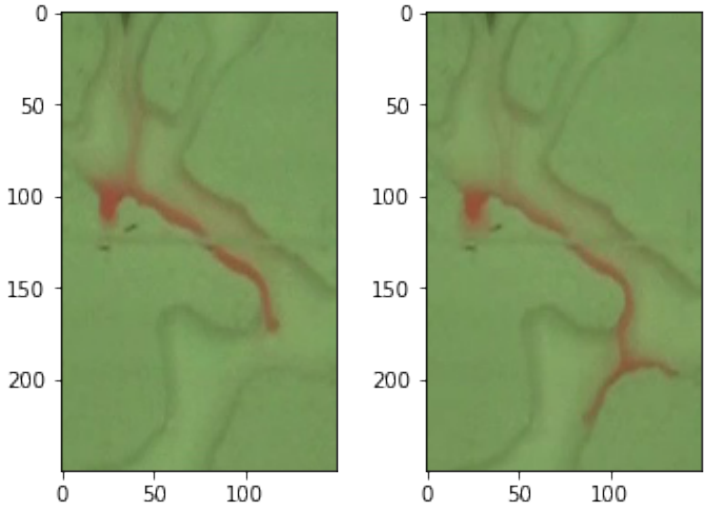

(a) Particles falling straight down (b) Particles sticking to the wall

Figure 4.26: Example of the particles falling down straight initially, and a few seconds later when particles stick to the wall

The travelled distance was mainly determined by the fact that the particles encountered a larger cavity which could not be entirely filled and spilled over due to the large volume of the cavity. Too many particles were captured in earlier cavities, resulting in a too low volume of particles to fill up the last cavity in which particles got trapped. Unfortunately, at larger concentrations (3.5% and 5%), where perhaps a sufficiently large number of particles was present to overcome the last cavity, leakage of particles occurred between the pore network and the covering acrylic block. The particles thus leaked from the cavities between the pore network and the wall, prematurely ending the experiment as particles leaked from the experimental setup.

Remarkable was the larger average velocity of the swarm at $c_0 = 3.5\%$ and $c_0 = 5\%$ in pore geometry 2. One possible explanation may be that there were no early encountered cavities in which particles got stuck. Consequently, particles could not leak between the pore network and the acrylic block, and their number remained large, possibly leading to the larger observed velocities. This would fit the observation that larger concentrations, thus more particles lead to an increased velocity. The change in channel geometry in the pore geometry 2 was most likely not responsible for the larger velocities at higher concentrations, since this would mean that also the lower concentrations should have experienced increased velocities compared to pore geometry 1.

4.2. Particle leakage results

4.2.1. Smooth fracture

The number of particles in a blob as estimated from both the tail and varying radius and fixed radius blob method (Figure 4.27) in general showed a clear declining trend, indicating that the blob lost particles as is travelled through the fracture. The tail method generally produced more stable leakage rates, whereas the blob method showed more flashy results.

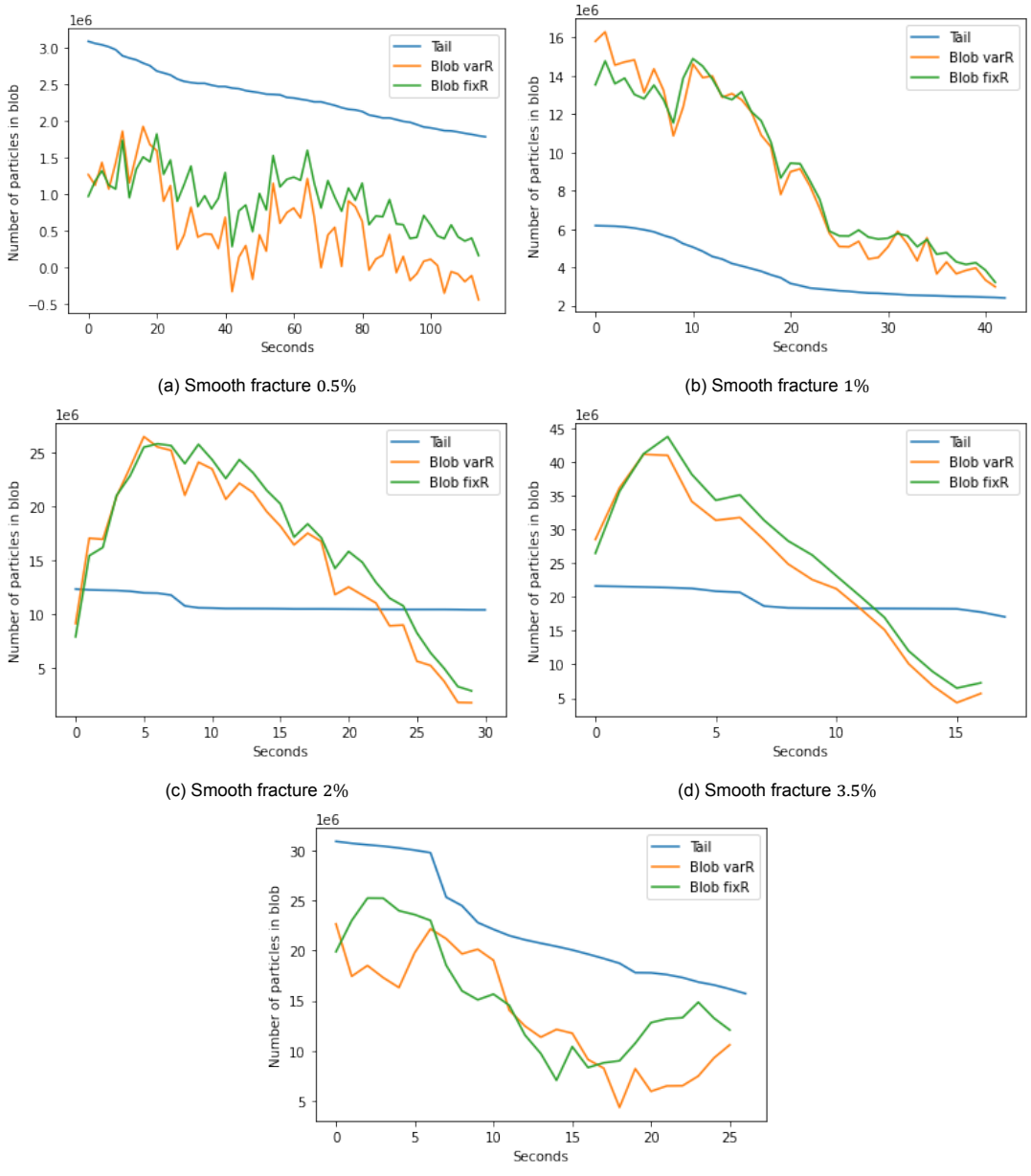

(a) Smooth fracture 0.5%

(b) Smooth fracture 1%

(c) Smooth fracture 2%

(d) Smooth fracture 3.5%

(e) Smooth fracture 5%

Figure 4.27: Smooth fracture, number of particles in the blob as estimated via the tail method and variable and fixed circle radius via the blob method

The differences between the varying circle and fixed circle radius in the blob method were small. Presumably, this was the case since both methods assess the colour intensity at the core of the blob, which was significantly more colour intense than the baseframe. Consequently, all pixels in the circle were used in computation of the average colour intensity. Since the average value of the colour intensity was used to estimate the number of particles, the effect of the varying area was compensated for. If the fixed radius was taken such that it did not exceeds the blob bounds, both methods thus lead to similar results.

Since results between the varying radius and fixed radius differed so little, they were regarded as one method. It was chosen to use the results of the fixed radius blob method to represent the blob analysis method, as the fixed radius did not produce a negative number of particles in the $c_0 = 0.5\%$ experiment.

There were however noticeable differences between the tail and the blob analysis method. Firstly, the tail method started at the theoretical correct number of initial particles. Since the number of particles in the blob method was based on a fitted trend line and data points either lied above or below the trend line, the number of particles at the start did not match the theoretically determined values for the blob method.

Moreover, the blob method predicted much larger leakage rates than the tail method, as seen by the steeper decline in number of particles. This feature may be caused by the increasing width of the blob as it progressed through the fracture. The particles inside the blob were then distributed over a larger area, leading to a lower colour intensity of the blob. As a result, the computed number of particles reduced, even if the blob had not lost any particles. The combined effect of particle leakage with widening of the swarm could cause the steep decline in number of particles that was observed.

The number of particles in the blob at 2% and 3.5% (Figure 4.27c, Figure 4.27d) showed a noteworthy feature; the number of particles in the blob increased rather than decreased. The cause of this phenomenon was the tail that caught up with the leading blob, an observation also made by Machu et al. (2001). The hypothesis was that the blob slowed down after injection due to an increase in width and thus drag, allowing the particles in the tail to catch up and merge with the blob. Analysis of the velocity and width at 2% and (Figure 4.28a) confirmed this idea. At 3.5% however, no reduction of velocity of the blob is visible (Figure 4.28b), questioning the aforementioned hypothesis. Catching up of the tail could also be attributed to a *slipstream* effect. Particles in the tail moved in the wake of the larger blob in front, which reduced their hydrodynamic drag and allowed them to catch up with the blob.

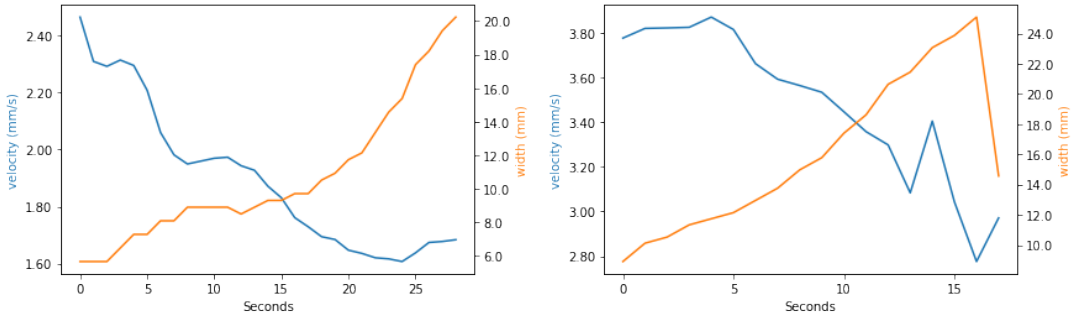

(a) Smooth fracture, 2%

(b) Smooth fracture, 3.5%

Figure 4.28: Smooth fracture, velocity and the width of the blob over time at 2% and 3.5% initial particle concentration

It should also be noted that the particle leakage rate as predicted by the tail method at the end of the 1% and 2% concentration experiment was close to zero and the number of particles in the blob therefore approximately constant. No particles leaking from the blob must mean that there was no tail in which the number of particles could be estimated. Indeed, upon checking the video footage, blobs appeared to lose their tail at some point, an observation also reported by Machu et al. (2001).

The fact that the particle leakage rate in the tail method followed a more slowly decreasing line over time matched the observation in the experiment that the tail became thinner until it became disconnected and are also in line with findings of Machu et al. (2001), who also mentioned that ”the tail becomes increasingly thinner as the drop continues to fall” and consequently, the particle leakage rate via the tail should decline.

Moreover, the tail method produced much more stable leakage rates, which was also observed in the experiments. Although the thickness of the tail differed, which may indicate a varying particle leakage rate, the leakage rate proposed by the blob method was too flashy. Despite the fact that both methods produce a percentage-wise particle leakage rate that declined with increasing concentration (Metzger et al., 2007), the blob method estimated a too large percentage particles lost (Figure 4.29b), when optically checked in the video footage. The lower percentage wise particle leakage rates in the tail method (Figure 4.29a) were more plausible.

Of the two methods, the tail analysis method was presumed to provide the best estimate for the particle leakage rate in the smooth fracture.

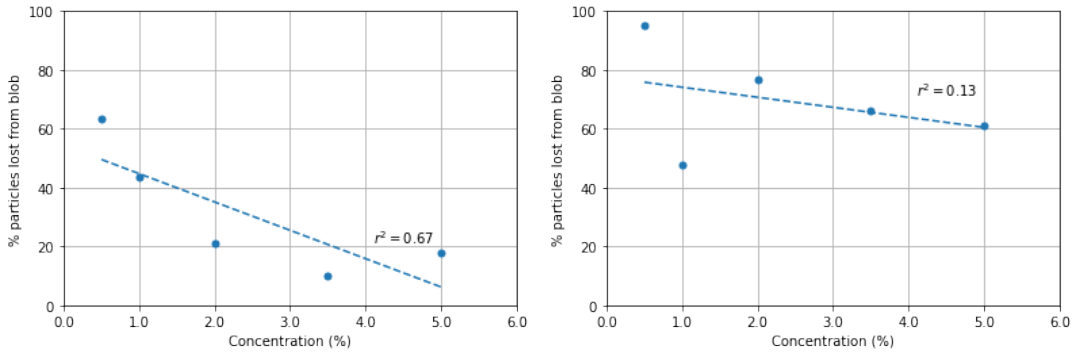

(a) Tail method

(b) Blob method

Figure 4.29: Smooth fracture, percentage of particles lost from the blob compared to the initial number of particles

4.2.2. Rough fracture

Both the tail and blob analysis method clearly showed that the number of particles in the blob decreased over time (Figure 4.30).

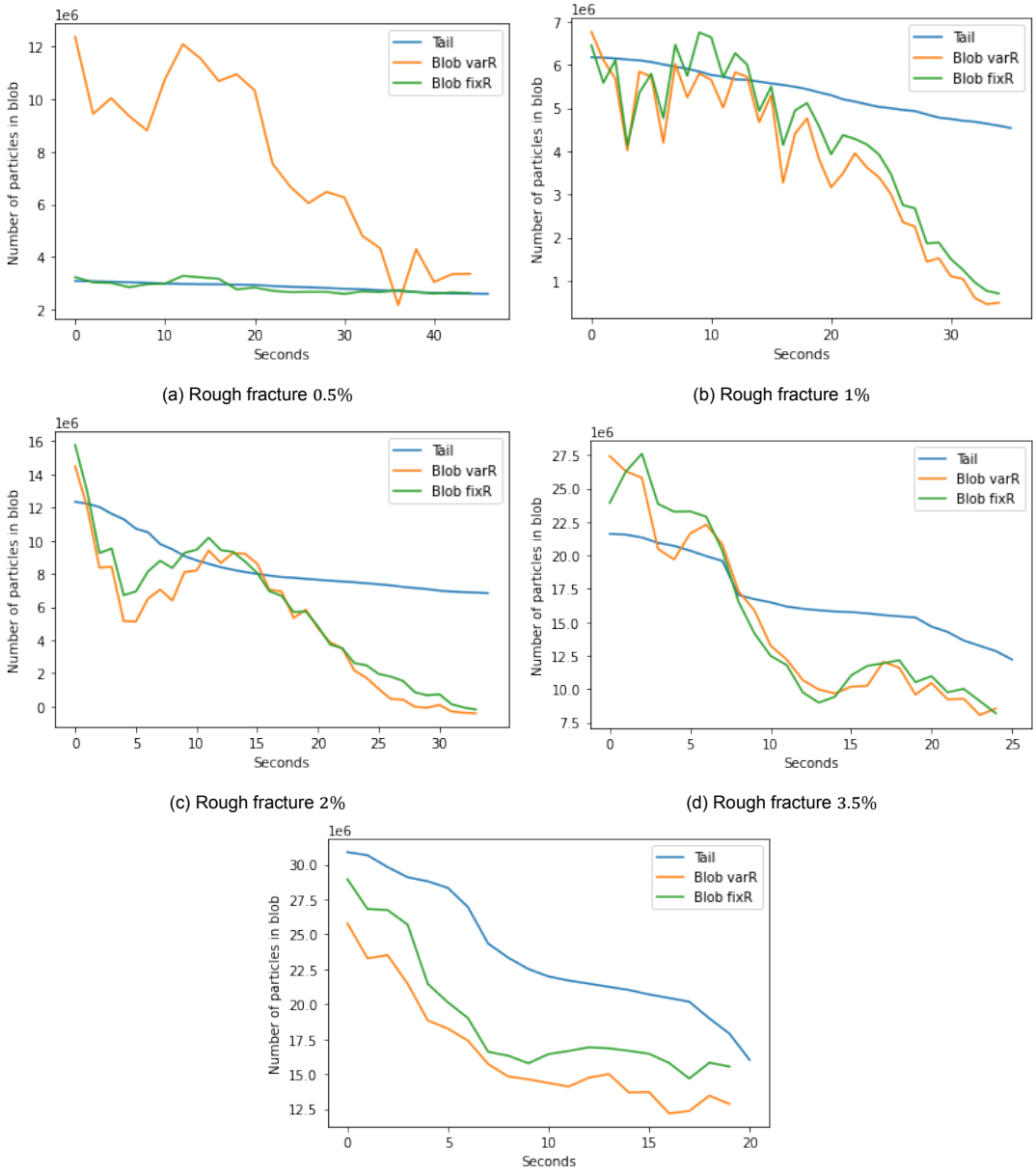

(a) Rough fracture 0.5%

(b) Rough fracture 1%

(c) Rough fracture 2%

(d) Rough fracture 3.5%

(e) Rough fracture 5%

Figure 4.30: Rough fracture, number of particles in the blob as estimated via the tail method and variable and fixed circle radius via the blob method

As seen previously, the tail method produced more stable leakage rates, while the blob method showed more smaller and larger peaks. Remarkable was the low number of particles in the blob determined by the blob method at the end of the experiment. This was so extreme, that the blob method estimated a negative number of particles in the $c_0 = 2\%$ experiment in the last two seconds.

The differences between the varying circle radius and the fixed circle radius in the blob method were small, except at the 0.5% initial particle concentration (Figure 4.30a). The blob in this experiment was exceptionally narrow and consequently the fixed circle included some parts outside the swarm boundary, lowering the average colour intensity and thus the number of particles. Since a portion of the background colour was included, the average colour intensity was much more stable and therefore the number of particles in the blob was too.

A note that should be made for the $c_0 = 0.5\%$ fixed radius blob method is that the average colour intensity data point locally had a poor fit to the trend line (Figure F.2b, RF set 1), leading to a significantly larger underestimation of the number of particles than usual. Because the trend line estimated close to zero particles in the blob, this was compensated for by adding $3E06$ (approximately the theoretical initial number of particles) to the number of particles in the blob.

Because the varying and fixed radius in the blob method provide highly similar results, but the fixed radius produced better results at $c_0 = 0.5\%$, it was chosen to use the fixed radius as representative results for the blob method.

Difference between the tail and blob analysis method were still present, with the number of particles in the blob analysis method declining at larger rates than for the tail analysis method. As with the smooth fracture, this may be caused by widening of the blob which reduced its average colour intensity. As a result, the blob method estimated significantly more particle leakage from the blob than the tail method (Figure 4.31), with unrealistic leakages rates up to 101% in the blob method.

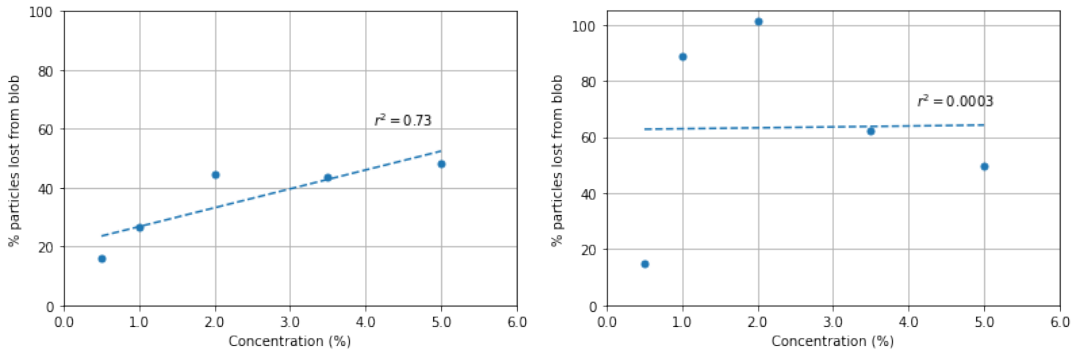

(a) Tail method

(b) Blob method

Figure 4.31: Rough fracture, percentage of particles lost from the blob compared to the initial number of particles

The leakage rate over 100% may be explained by the relationship between the colour intensity and the number of particles (Appendix F, Figure F.2). If the colour intensity dropped below the value that was related to zero particles, it was estimated that a negative number of particles was present, leading to a leakage rate over 100%. This may either be due to a poor local fitted trend line or the spreading of the swarm in width and depth leading to low colour intensities.

The fading of the tail and thus a reduction in particle leakage was also better captured in the tail analysis method (Figure 4.30c), visible by the near constant number of particles in the blob at the end of the experiment. These described differences, together with a more stable leakage rate that matched experimental observations, make that the tail method was most probable to provide plausible estimates for the number of particles in the blobs.

4.2.3. Pore network

The determination of particle leakage rate in the pore network lead to peculiar results, with unrealistic numbers of particles and sudden peaks or declining trends of particle numbers left in the system. The particle leakage rate was thus not used, since due to the comprehensiveness of other elements of this study, no new attempt was made to estimate particle leakage in the pore network.

While no clear reason for the random peaks could be found, the unrealistic number of particles and the declining number of them trapped in the pore network could be explained. The declining number of particles may have been caused by the settling of particles on a pore wall, where they would spread out more evenly over the 'depth' of the pore (as seen from the camera). This could have resulted in the particles in the back not being accounted for properly via colour intensity, thus resulting in a declining number of particles over time.

The unrealistic number of particles may be caused by leakage of particles between the printed pore network and the covering acrylic block, that did not make a water-tight fit. At larger concentrations, leakage became more pronounced and this thin leaking layer was also accounted for in the number of particles trapped in the system. The larger area of a thin layer of particles may have resulted in overestimating the number of particles that were left in the pore network.

4.3. Modelling results

Modelling the velocity of swarms required an input of the number of particles in the blob. It was previously shown that the tail analysis method produced better results in both the smooth and rough fracture. The number of particles in the blob as estimated by the tail analysis method was thus used in the modelling of colloidal swarms.

4.3.1. Smooth fracture

The velocity of the swarm determined by swarm analysis and as computed with the Hadamard & Rybczynski (HR) model (Equation 3.2) are compared in Figure 4.32.

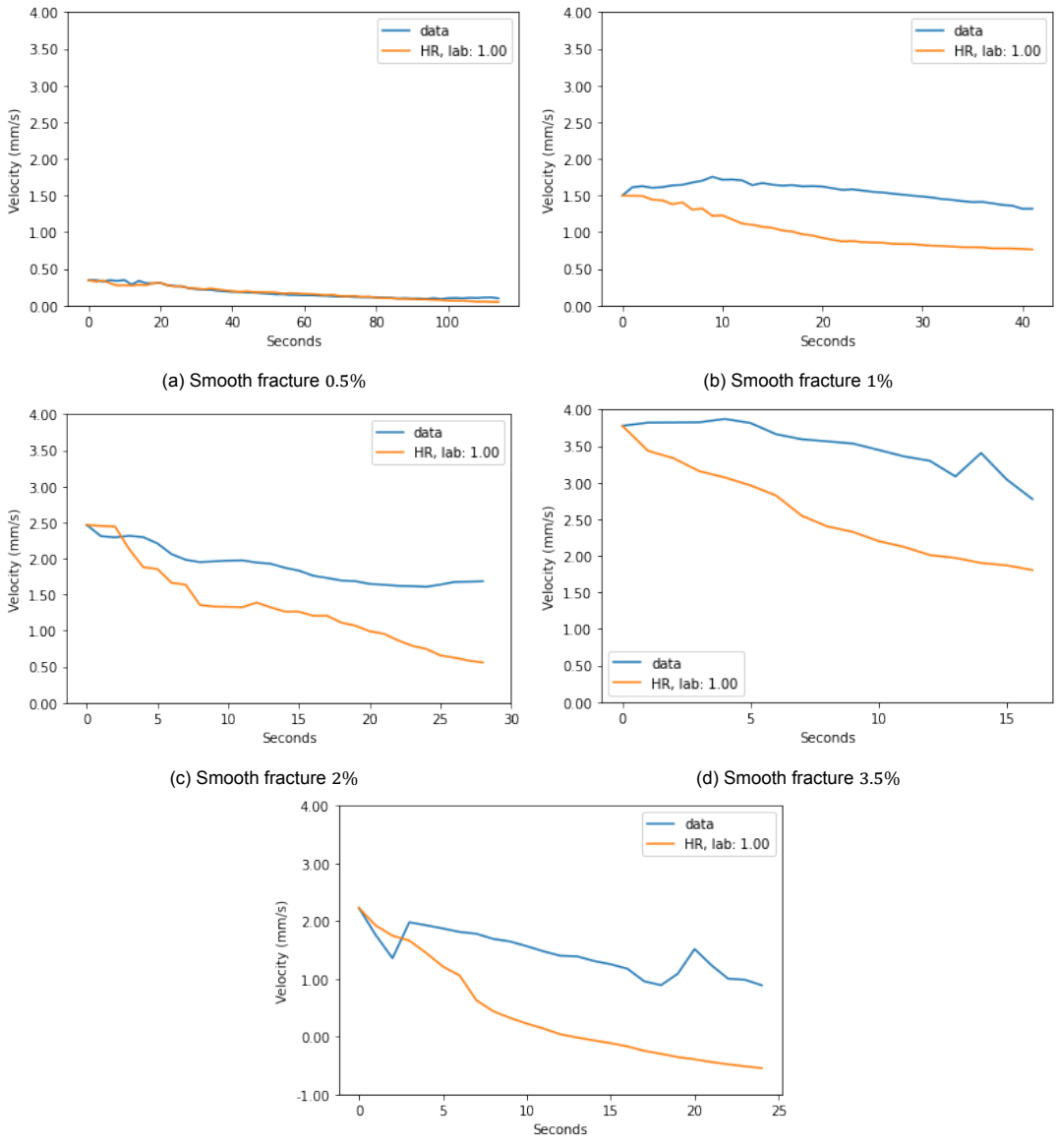

(a) Smooth fracture 0.5%

(b) Smooth fracture 1%

(c) Smooth fracture 2%

(d) Smooth fracture 3.5%

(e) Smooth fracture 5%

Figure 4.32: Smooth fracture, velocity based on experimental data and the HR model

It should be noted that the HR model velocities were offset to start at the same velocity as the data to enable comparison between the two. At $c_0 = 5\%$, this offset, combined with the steep slope of the HR velocity, caused the HR velocity to end up at a negative velocity (Figure 4.32e). Between the bounds of $1 \leq \lambda \leq 1000$, the HR model fitted the data best if $\lambda = 1$. At all initial particle concentrations except for 0.5%, the HR model swarm velocity showed a steeper decline than the data, resulting in a poor fit. This was also the reason that the $\lambda = 1$ for these experiments; not because it was the best fit, but because the bounds did not allow this value to drop further into the physically impossible domain.

The offset required to start the HR model at the data velocity may have been caused by an error in determination of the blob width. The too steeply declining velocity could be caused by an error in the leakage rate estimate, a faulty λ estimate or not accounting for the confining forces of the fracture wall on the swarm. These hypothesis were tested and discussed in the following.

If the width, R, of a blob was wrongly determined during swarm analyses, the computed HR swarm velocity would be offset. A too large determined width would lead to a lower velocity, while a too small determined blob width leads to a larger HR velocity. The required offset for the HR velocity to match the data, along with the required error in blob width determination (Table 4.1) showed that the error should be improbably large and highly inconsistent. An error in blob width determination during swarm analyses was thus an unlikely cause for the offset that was observed between the HR model velocity and the observed swarm velocity.

Table 4.1: Smooth fracture, the required offset for HR velocity to start at the data velocity. Negative offset means HR velocity had be adjusted downwards to match data

	0.5%	1%	2%	3.5%	5%
Offset (mm/s)	-0.055	0.578	-0.032	0.994	-0.922
error in R (%)	-16	38	-1	26	-40

An error in estimation of the number of particles in a blob, N_b, would have resulted in an error in the HR velocity as can be seen in Equation 3.2. A too large large particle leakage rate would result in a too quickly declining velocity. However, even if Nb was set to be constant and equal to the initial number of particles, the HR velocity still declined too rapidly, having a velocity lower than observed. The mismatch between the HR velocity and data could thus not be explained by an error in the leakage rate.

By increasing the estimate of λ, the HR velocity decreased. If λ increased from 1 to 1000, the denominator of Equation 3.2 merely changed from $5 * R$ to $6 * R$, from which it followed that the HR velocity only decreased slightly. The λ estimate did therefore not greatly affect the HR velocity. Moreover, by increasing λ, the HR velocity decreased, whilst it was already under predicting the observed velocity. A lower value of λ (below 1) was also not viable, since this would mean that the viscosity of the suspension of particles is lower than that of the water. Thus, the λ estimate was not the cause of the mismatch between the HR model velocity and the data.

In the smooth fracture, the blob was forced to move between two closely placed walls. The confining forces of the wall enhanced blob velocity (Boomsma and Pyrak-Nolte, 2015) and this may explain the larger observed swarm velocities than predicted by the HR model. This hypothesis could be tested by looking at the open tank experiments, where confining forces were small. As was discussed in Subsection 2.7.1, the tail analysis method could not provide particle leakage rates for the majority of the open tank experiments. However, 5 open tank experiments could be analysed, hence also modelled.

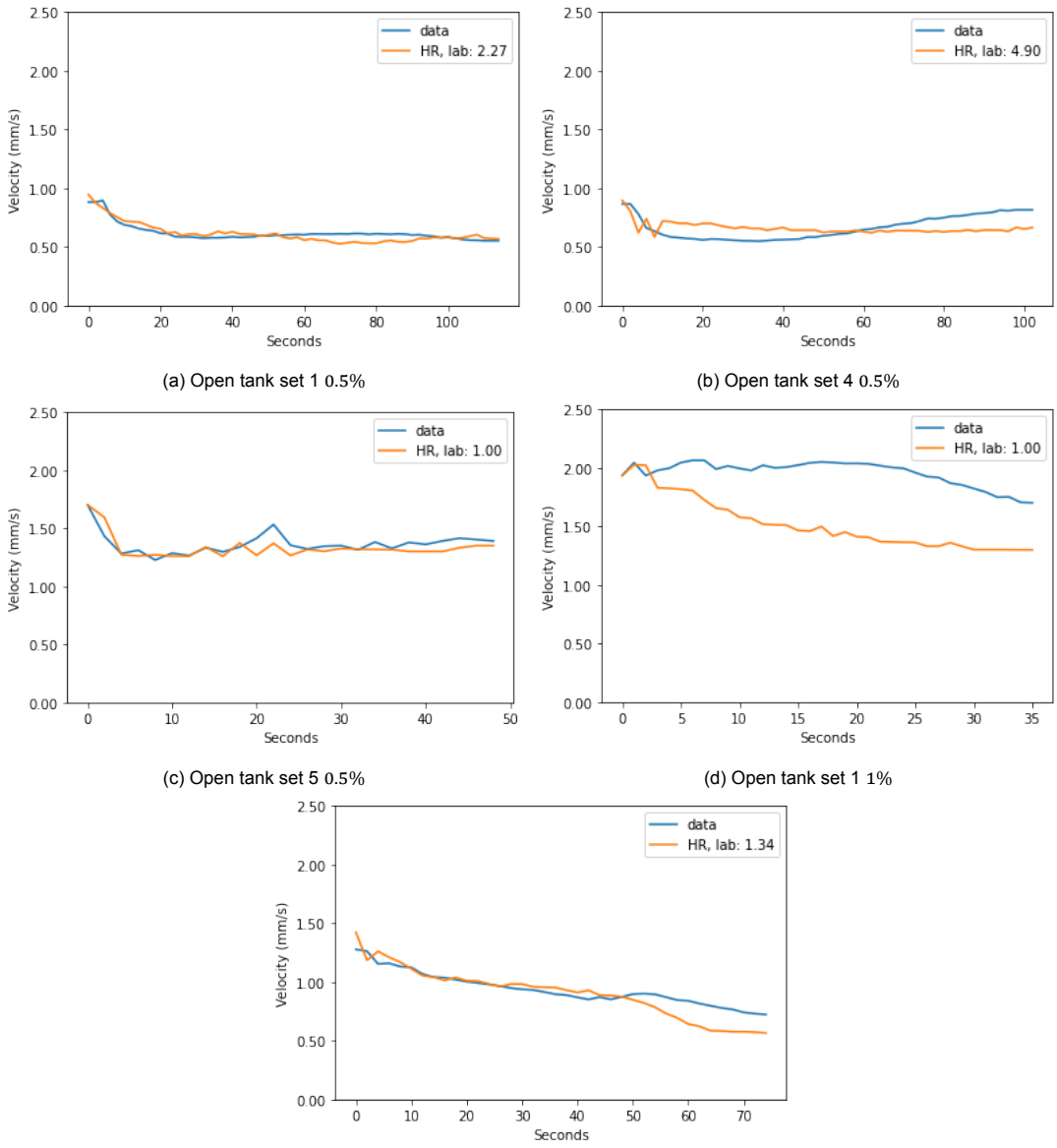

(a) Open tank set 1 0.5%

(b) Open tank set 4 0.5%

(c) Open tank set 5 0.5%

(d) Open tank set 1 1%

(e) Open tank set 4 1%

Figure 4.33: Open tank, velocity based on experimental data and the HR model

From Figure (4.33) it became clear that the HR model can be well fitted to the open tank data, even without the bounds that were set on the value of λ (except for 0.5% Open tank set 5, Figure 4.33c), although λ did vary significantly between experiments.

It appeared that the lack of confining forces to enhance the velocity caused the HR model to accurately fit the velocity data. Figure (4.33) strongly implied that it was indeed the case that confining forces caused the mismatch between HR and data velocity in the smooth fracture.

4.3.2. Rough fracture

In the rough fracture experiments, the HR model velocity and data showed a remarkably good fit (Figure 4.34). Note that the HR model again was given an offset.

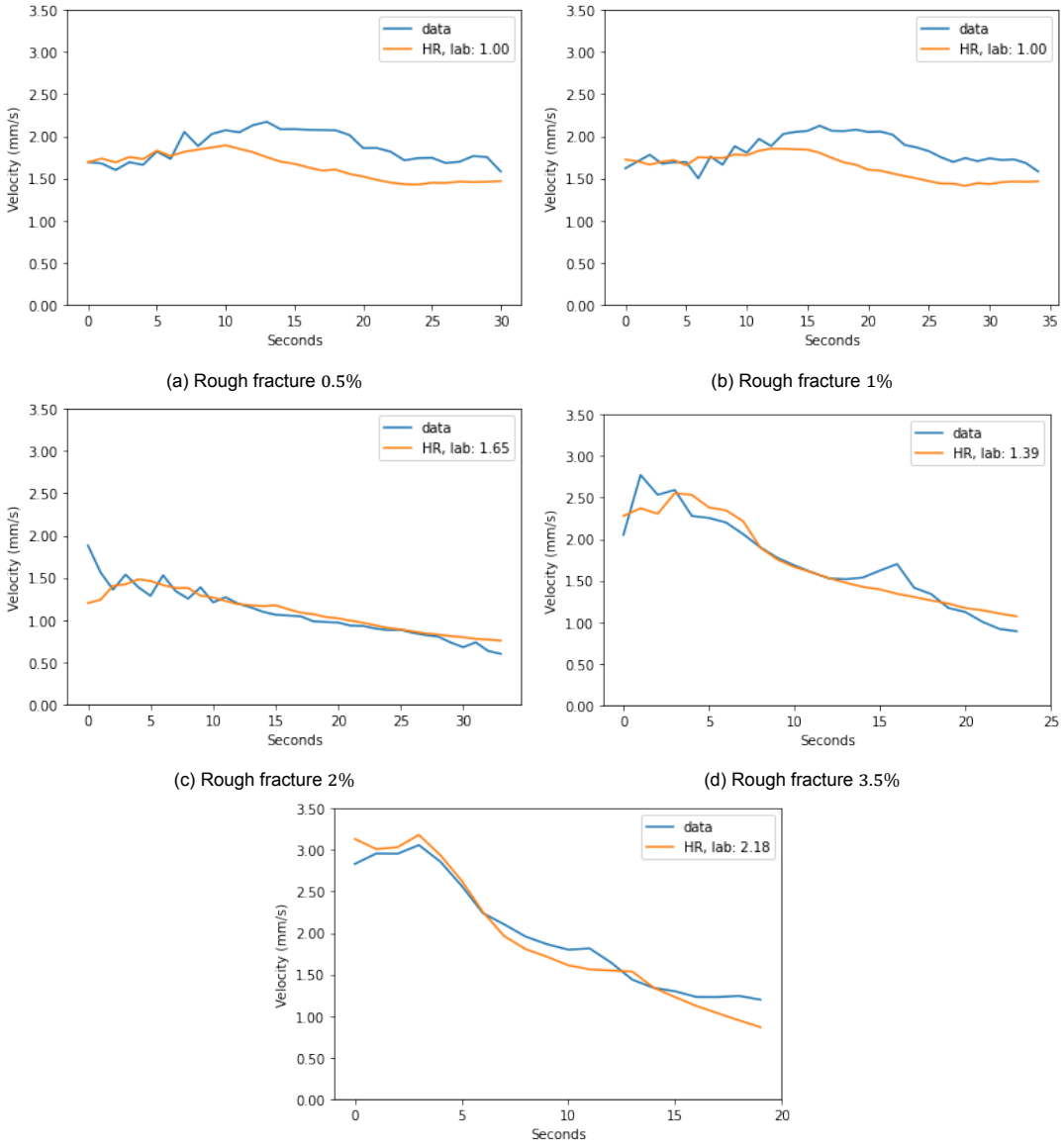

(a) Rough fracture 0.5%

(b) Rough fracture 1%

(c) Rough fracture 2%

(d) Rough fracture 3.5%

(e) Rough fracture 5%

Figure 4.34: Rough fracture, velocity based on experimental data and the HR model

Table 4.2: Rough fracture, the required offset for HR velocity and data to start at the same velocity. Negative offset means HR velocity had be adjusted downwards to match data

	0.5%	1%	2%	3.5%	5%
Offset (mm/s)	0.860	1.005	0.500	0.388	-0.222

At 2% initial particle concentration and higher, λ values were found within their bounds that fit the data best. The HR swam velocity was substantially better able to match the velocity data in the rough fracture than in the smooth fracture.

This result was in line with the finding that the confining forces in the smooth fracture enhanced velocity, leading to the HR model to under predict the observed velocity. The rough fracture imposed more drag forces on the blob due to the roughness of the wall. The blob velocity was thus not only affected by confining forces, but also by drag forces, counteracting the increased swarm velocity. Consequently, the HR model was better able to fit the observed velocity. It was thus evident that the rough fracture imposed more drag forces on the swarm, inhibiting its velocity.

4.3.3. Pore network

The ratio of the swarm velocity at a given initial particle concentration ($c_{0,i}$) over the swarm velocity at $c_0 = 0.5\%$ as a function of the initial particle concentration is presented in Figure 4.35 below.

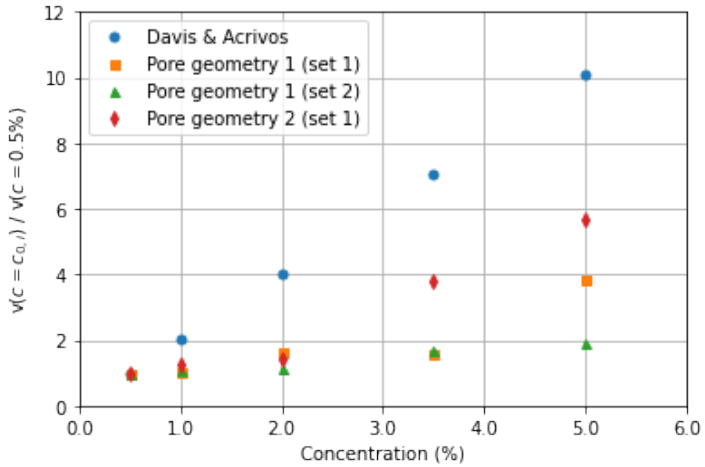

Figure 4.35: Pore network, concentration versus the ratio of velocity at a given concentration over velocity at $c_0 = 0.5\%$

The ratio of velocity of the swarm as computed with the Davis & Acrivos (DA) equation (Equation 3.6) showed a linear increase with concentration. This trend was also observable in the experimental results, but for the fact that the linear increase was less steep. The experiments thus showed a lower increase in velocity with concentration. In general however, the ratio was in the same order of magnitude as experimental results. The velocities predicted by DA at larger concentrations were thus relatively too high, or the velocity at $c_0 = 0.5\%$ was predicted too low. For example, a factor 1.5 larger velocity at $c_0 = 0.5\%$ in the DA model would already result in the model having an excellent fit to the swarm velocity in pore geometry 2.

The mismatch at larger concentrations may have also been caused by the particles leaking between the pore network and the acrylic plate. The leakage of particles caused their numbers to reduce, and as can clearly be seen in Figure 4.35, this would lead to a reduction in velocity. It may thus not be the model that is overpredicting the ratio, but the experiments that resulted in too low velocities due to particle leakage from the experimental setup.

It should be noted that these results were a global assessment of the effect of concentration on propagation of colloidal swarms in the pore network. Nevertheless, the model did show that the velocity of colloidal swarms in a pore network could reasonably well be described by the the DA model.

5

Conclusions and Recommendations

5.1. Conclusions

The formation and behaviour of colloidal particle swarms can strongly affect the transport rate of colloidal particles. This may have important implications for systems containing these particles, such as the application of DNA tracers in fractured soils or the transport of colloidal contaminants in urban stormwater runoff through porous media. Therefore, the research question of this thesis was the following: what is the effect of particle concentration on the behaviour of colloidal swarms in varying confining geometries?

To answer this question, the effect of concentration on swarm behaviour was studied in terms of the swarm velocity, swarm width, point of bifurcation and leakage rate of the swarm (or blob in case of a spherical swarm). To this extent, various concentrations of colloidal particles were injected in three geometries that were suspended in a stagnant column of water; a smooth fracture, a rough fracture and a pore network. The leakage rate of a blob was assessed to model the swarm velocity, since the velocity of the blob was related to the number of particles in it. These parameters were obtained through self-developed Python analysis of captured video footage during the injection experiment. The particle leakage rate from the blob was estimated via two methods, relating either the colour intensity of the tail or the colour intensity of the blob to the number of particles present in the blob. Modelling of the velocity of swarms was done for better interpretation of results. In the smooth and rough fracture this was done with the Hadamard & Rybczynski (HR) equation. In the pore network, the velocity of the swarm was described using equations that could be interpreted as the Boycott effect, where inclined pore throats lead to more rapid particle settling.

The influence of concentration on swarm behaviour

In both the smooth and rough fracture, the average velocity of the swarm showed a slight decreasing trend with increasing concentration. The average velocity of swarms in the smooth and rough fracture were similar. In the pore network however, a strong positive linear relationship between the average swarm velocity and particle concentration was found. This was caused by a larger mass of the swarm due to an increased number of particles and the confining geometry inhibiting swarm widening in contrast to the fracture experiments.

A positive linear relation was found between the average width of a swarm and the particle concentration, in both the smooth and rough fracture. Wider swarms experienced lower velocities, presumably due to increased hydrodynamic drag forces imposed on the swarm. This was in line with the observed slightly decreasing average swarm velocity with increasing concentration. In the pore network, the width of the swarm was not measured since the swarm was confined by the pore geometry.

The distance the swarm travelled before bifurcation took place did not show a clear relationship with the particle concentration for either the smooth or rough fracture. However, in both fractures, the distance to bifurcation could be linked to the average settling velocity of the swarm, with larger velocities leading to greater distances before bifurcation occurred. In the experiments of this thesis, swarms did not bifurcate at a threshold velocity, but rather at a threshold width that increased with concentration. Swarms bifurcated at a threshold width independently of confining geometry. Bifurcation was not investigated in the pore network, since the swarm movement was fully guided by the geometry of the pore network, following the pore wall and filling up and spilling over cavities.

Particle leakage rate

In both fractures, the particle leakage rate via analysis of the tail provided better results than analysis of the blob. The particle leakage rates as estimated via the tail analysis were used in modelling the velocity of swarms in the smooth and rough fracture. In the pore network, particle leakage from the swarm could not be assessed due to significant particle leakage from the experimental setup.

Modelling of swarm velocity

The HR model did not fit the observed swarm velocity in the smooth fracture well, because the confining forces of the fracture walls enhanced swarm velocity, which was not accounted for by the HR model. However, the HR model did fit well to the observations in the rough fracture, since the increased drag forces of the wall on the swarm counteracted the enhanced velocity resulting from the confining forces of the walls. The effect of particle concentration on the average swarm velocity in the pore network was sufficiently well modelled in terms of the Boycott effect.

5.2. Recommendations

To further investigate the behaviour of colloidal particle swarms, it is recommended to further build upon this research, improve the experimental setup, enhance the modelling of swarm velocity and facilitate the translation to a natural system.

Recommendations regarding the research question

Laminar flow conditions may be introduced to the experiments to enable better interpretation of results for natural systems, as these systems are often characterized by non-zero flow conditions. In the smooth and rough fracture swarms may either fall apart due to the increased advection term, but may also benefit from the reduced drag imposed on the front of the swarm. Consequently, swarms could widen less rapidly and bifurcate after a longer period, resulting in more stable swarms. In the pore network, laminar flow may create preferential flow paths and dead-end pores that enhance swarm transport through the pore network.

Additionally, a more simple pore network may be used. Two pore network geometries of similar geometric complexity were tested in this thesis, where the colloidal swarms had trouble travelling through this network. A simpler network provides a better gradual transition to the complex pore geometry experiments to more clearly investigate the behaviour of swarms in the pore network.

More detailed research on swarm behaviour after bifurcation in the fractures may be useful to better predict the longevity of swarm effects. This study has mainly focused on swarm behaviour in confining geometries up to the point of swarm bifurcation, but swarms may bifurcate multiple times and bifurcated clusters also experience large velocities.

Recommendations regarding the experimental setup

To further improve the reliability of experimental results, more experiments may be performed to increase robustness of data so statistical analysis may be performed on these chaotic systems. Also, the rough fracture aperture may be increased to ensure that similarities in the smooth and rough fracture are not due to the small fracture aperture of the rough fracture. Moreover, the pore network should be made watertight, so that no particles can leak from the experimental setup in the pore network. Furthermore, placing an extra camera to image swarms from the side enables the analysis of bifurcation of swarms in two dimensions, which will benefit the evaluation of particle leakage rates from a swarm.

Recommendations regarding the modelling of swarm velocity

The HR model may be expanded upon by incorporating confining forces and drag forces resulting from the presence of fracture walls, such that the HR model can be used to describe swarm velocity in fractures. The modelling of colloidal swarms in the pore network may benefit from a simpler pore network geometry, as it allows for better investigation on how well the Boycott effect can describe swarm velocity in a pore network.

Recommendations regarding the translation to natural environment

Strong evidence has been put forward on the presence of colloidal swarms in fractures and porous media in laboratory conditions. The results of the fracture experiments should be compared to those of a field study. Both physical disturbances, such as more narrow and discontinued fractures, as well as chemical disturbances, such as changes in surface potential of both colloids and solid medium, may severely hinder colloidal swarms.

To establish if colloidal swarms can travel through porous media in natural environments, more research is required. Injection into a real porous medium, for example using colloidal contaminants, is a step in that direction.

It is however improbable that swarming effects will play a big role in urban colloidal contaminant transport in porous media. Firstly, urban contaminants are not injected as high concentration pulses and do thus not resemble performed experiments. Swarms may not form at all if the colloidal contaminants are too sparsely spread. Secondly, colloidal swarms may well not be able to travel through the pore network unscathed, since a porous medium may be geometrically too complex, trapping (large parts of) the colloidal swarm in pore cavities.

The formation of swarms with sparsely spread colloids in porous networks should thus be further investigated to evaluate if colloidal contaminant swarms can be expected to be present in natural systems. In addition, injection experiments in natural samples will better mimic these systems and therefore provide a more solid basis for further discussion and research into this matter.

A

Colloidal Particle Analysis

Particle count

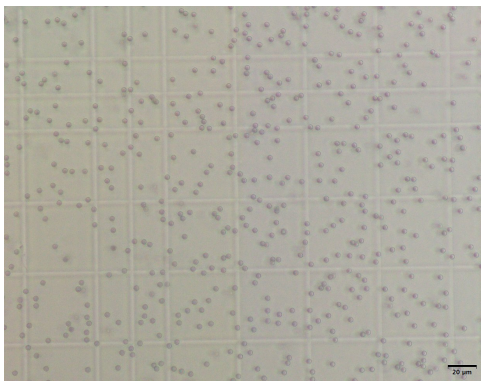

Figure A.1: Image of the 10 times diluted stock solution under a 400x magnification in a Neubauer chamber

Zeta potential and hydrodynamic radius

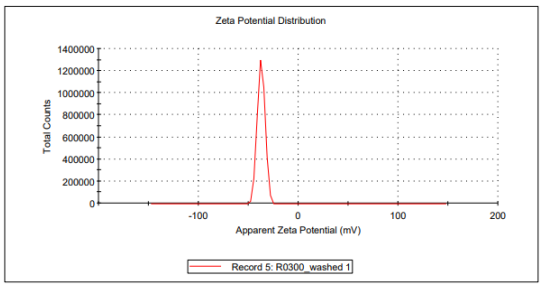

Figure A.2: Zeta potential of the washed particles

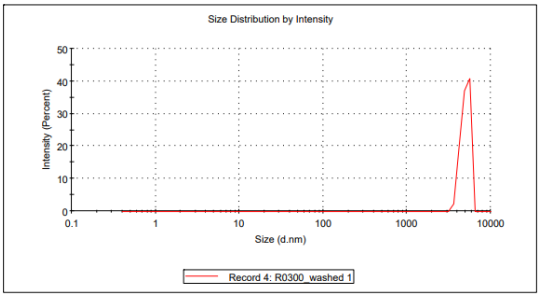

Figure A.3: Hydrodynamic radius of the washed particles

Figures A.2 and A.3 show the zeta potential and hydrodynamic radius of the washed particles. The particles were washed to remove the surfactant, since the surfactant may alter drop shape and surfactant gradients may lead to fluid motion (Stone, 1994). The washing method is described in Section 2.1.

B

Fractured Clay Images

Clay sample in the field

Figure B.1: The clay sample as found in Uithoorn on 29/05/2021

Desiccation process

Figure B.2: The clay sample after 50 hours (≈ 2 days) of drying outside

Figure B.3: The clay sample after 75 hours (≈ 3 days) of drying outside.

Final desiccated product

Figure B.4: The clay sample after 110 hours (≈ 4.5 days) of drying outside.

Figure B.5: The clay sample after 110 hours, tape measurer in cm for scale.

Figure B.6: The clay sample after 110 hours, detailed image of the largest fracture.

Figure B.7: The clay sample after 110 hours, detailed image of the largest fracture with tape measurer in cm for scale.

Figure B.8: The clay sample after 110 hours, detailed image of some smaller fractures at the side of the sample.

C

ZOAK Analysis

Images

Figure C.1: The piece of ZOAK after a slice had been cut off.

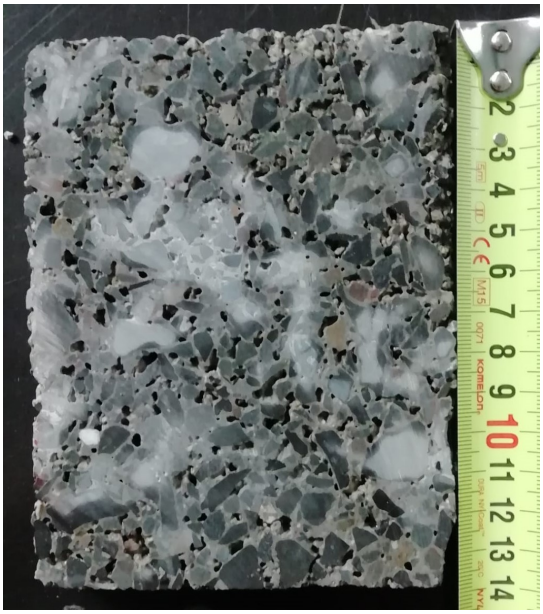

Figure C.2: The slice of ZOAK with tape measurer for scale.

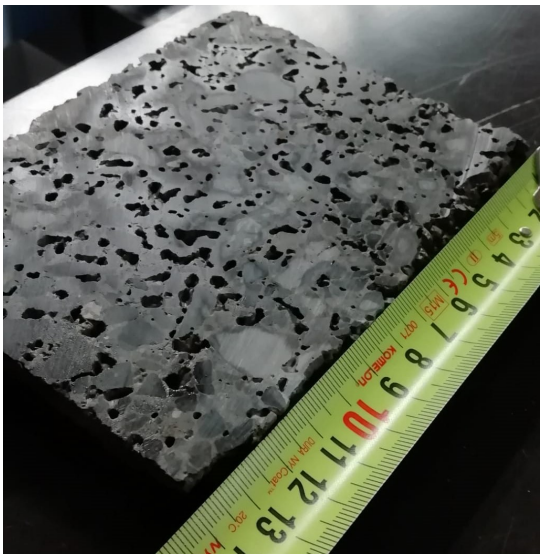

Figure C.3: The slice of ZOAK with tape measurer for scale, the pores are clearly visible.

Figure C.4: A detailed image of a large pore in the ZOAK

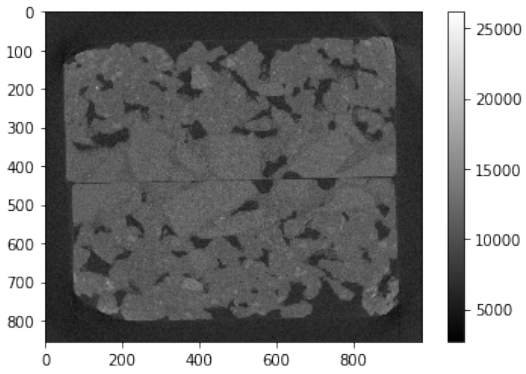

Figure C.5: Resulting top-view of the CT-scanned ZOAK sample loaded into Python. The small line in the middle clearly shows the two blocks joined together.

D

Relation between Injection Velocity and Swarm Velocity

A clear relationship existed for both the smooth and rough fracture, between the average swarm velocity and the injection velocity, which was measured as the velocity of the swarm during the injection period.

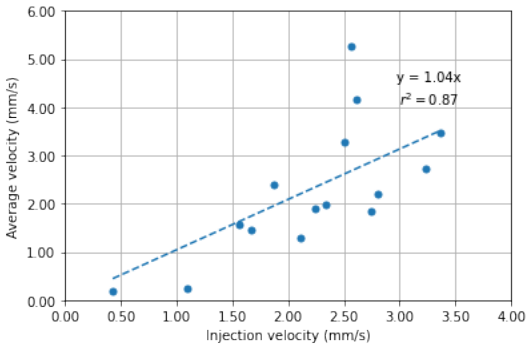

Figure D.1: Smooth fracture, injection velocity versus average velocity

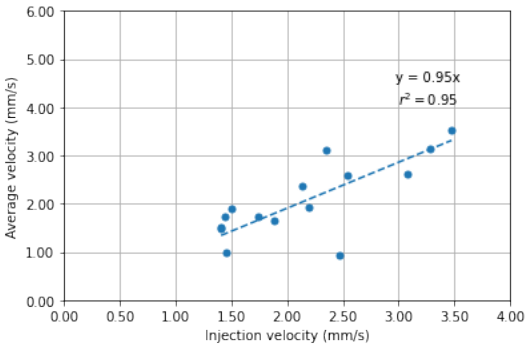

Figure D.2: Rough fracture, injection velocity versus average velocity

E

Open Tank Experiment Results

In the open tank experiments, at 0.5% initial particle concentration (table E.1), bifurcation did not occur in any of the 5 experiments. However, in the smooth fracture this did occur once, so the velocity at bifurcation at 1% initial particle concentration was used to normalise that data point.

Table E.1: Results from open tank experiments at initial particle concentration 0.5%. Velocity in mm/s, width and distance in mm

	0.5%				
Test no.	1	2	3	4	5
v_avg	0.70	0.77	0.66	0.77	0.62
v_bif	-	-	-	-	-
v_30mm	0.66	0.81	0.68	0.65	0.61
v_60mm	0.69	0.72	0.66	0.89	0.63
w_avg	1.6	1.4	1.3	2.0	1.8
w_bif	-	-	-	-	-
w_30mm	1.6	1.3	1.3	2.0	2.4
w_60mm	1.8	1.9	1.2	2.0	1.8
z_bif	-	-	-	-	-

Table E.2: Results from open tank experiments at initial particle concentration 1%. Velocity in mm/s, width and distance in mm

	1%				
Test no.	1	2	3	4	5
v_avg	1.04	0.48	0.66	0.74	0.70
v_bif	-	0.36	0.60	-	0.78
v_30mm	1.06	0.41	0.61	0.77	0.64
v_60mm	1.01	0.38	0.84	0.68	0.67
w_avg	1.5	2.5	3.3	2.1	2.3
w_bif	-	4.2	5.4	-	2.5
w_30mm	1.5	2.5	2.8	1.9	2.3
w_60mm	1.8	1.0	3.1	2.4	1.9
z_bif	-	41.6	58.8	-	60.8

Table E.3: Results from open tank experiments at initial particle concentration 2%. Velocity in mm/s, width and distance in mm

	2%				
Test no.	1	2	3	4	5
v_avg	0.99	1.01	1.28	0.89	1.08
v_bif	0.83	0.93	1.24	0.43	0.67
v_30mm	1.00	0.90	1.22	1.25	1.31
v_60mm	0.68	0.88	1.22	0.62	0.84
w_avg	4.1	3.6	3.7	4.4	4.0
w_bif	6.3	5.9	6.6	7.8	6.5
w_30mm	3.4	3.6	2.9	2.7	3.0
w_60mm	3.2	1.9	2.5	5.4	5.0
z_bif	47.9	43.2	51.5	57.8	66.5

Table E.4: Results from open tank experiments at initial particle concentration 3.5%. Velocity in mm/s, width and distance in mm

	3.5%				
Test no.	1	2	3	4	5
v_avg	1.09	1.36	0.81	1.09	0.63
v_bif	0.88	0.90	0.53	0.81	0.43
v_30mm	1.31	0.99	0.70	1.14	0.84
v_60mm	0.74	0.55	0.24	0.88	0.48
w_avg	3.7	2.7	4.2	4.3	6.0
w_bif	4.5	3.5	7.1	7.9	6.6
w_30mm	3.3	2.8	4.0	3.4	4.4
w_60mm	3.8	2.2	3.4	2.3	2.9
z_bif	53.4	30.4	41.6	50.2	44.4

Table E.5: Results from open tank experiments at initial particle concentration 5%. Velocity in mm/s, width and distance in mm

	5%				
Test no.	1	2	3	4	5
v_avg	0.70	0.90	0.78	0.96	0.96
v_bif	0.40	0.46	0.49	0.60	0.59
v_30mm	0.76	1.04	0.83	0.93	1.03
v_60mm	0.41	0.70	0.59	0.70	0.62
w_avg	3.9	4.6	4.2	3.5	3.1
w_bif	7.2	7.9	7.8	5.9	5.6
w_30mm	3.0	3.4	3.5	3.1	2.6
w_60mm	6.6	6.8	3.4	2.7	2.8
z_bif	62.6	65.6	53.2	50.4	54.4

F

Measuring the Particle Concentration via Colour Intensity

Tail analysis method

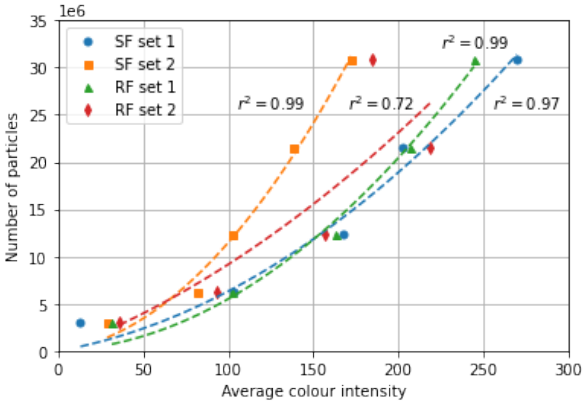

Figure F.1: Relationship between sum of colour intensity and number of particles just after injection

Figure F.1 shows the relationship between sum of colour intensity and the number of particles that was present. Per frame, all pixels with a colour value above the threshold, based on the maximum colour value in the baseframe, were summed to produce the sum of the colour intensity. The number of particles and the sum of the colour intensity followed a quadratic function through the origin. This showed that there was a 3D effect, since the swarm could also develop in the depth component as viewed from the camera. This was confirmed by the open tank experiments, in which swarms would bifurcate in the depth component also. The bifurcated clusters would then hide behind the front-most cluster (as seen from the camera), were they could not be observed, up to the point where one of the bifurcated clusters appeared above the swarm. The analysis then concluded that a large number of particles had leaked, whilst in reality it was the deeper bifurcated cluster that showed up from behind the front-most one. This method was therefore not suited for bifurcating open tank experiments.

Blob analysis method

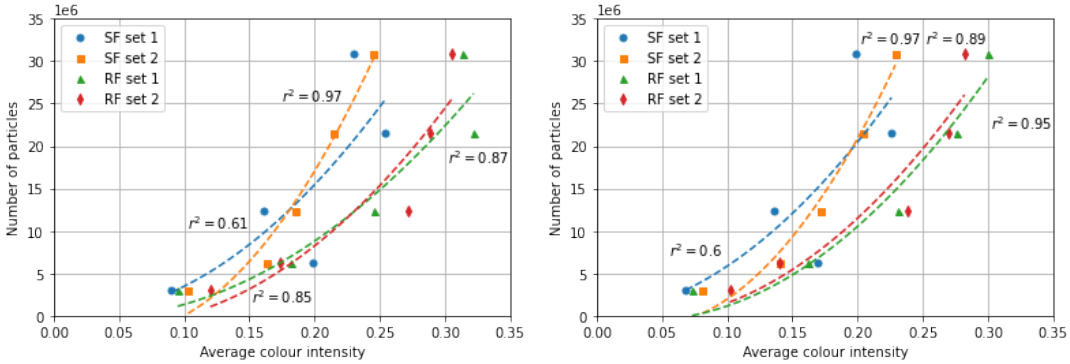

(a) Varying radius

(b) Fixed radius

Figure F.2: Relationship between average colour intensity and number of particles just after injection

G

Preparatory Experiments

To explore the existence of an optimal fracture aperture, preparatory experiments were performed with salt density fluxes in the macro-model. Although no colloidal particles were used, these results still provided insight in cluster behaviour for various fracture apertures and allowed optimization of analyses techniques. At all apertures, cluster analyses code was run until clusters were too diffuse to be detected. This occurred after 351, 400 and 230 frames for the $4\ mm$, $10\ mm$ and $16\ mm$ apertures respectively. Not all experiments started at the same number of frames, but this had to do with the timing between start of filming and start of injection and did not affect cluster analyses.

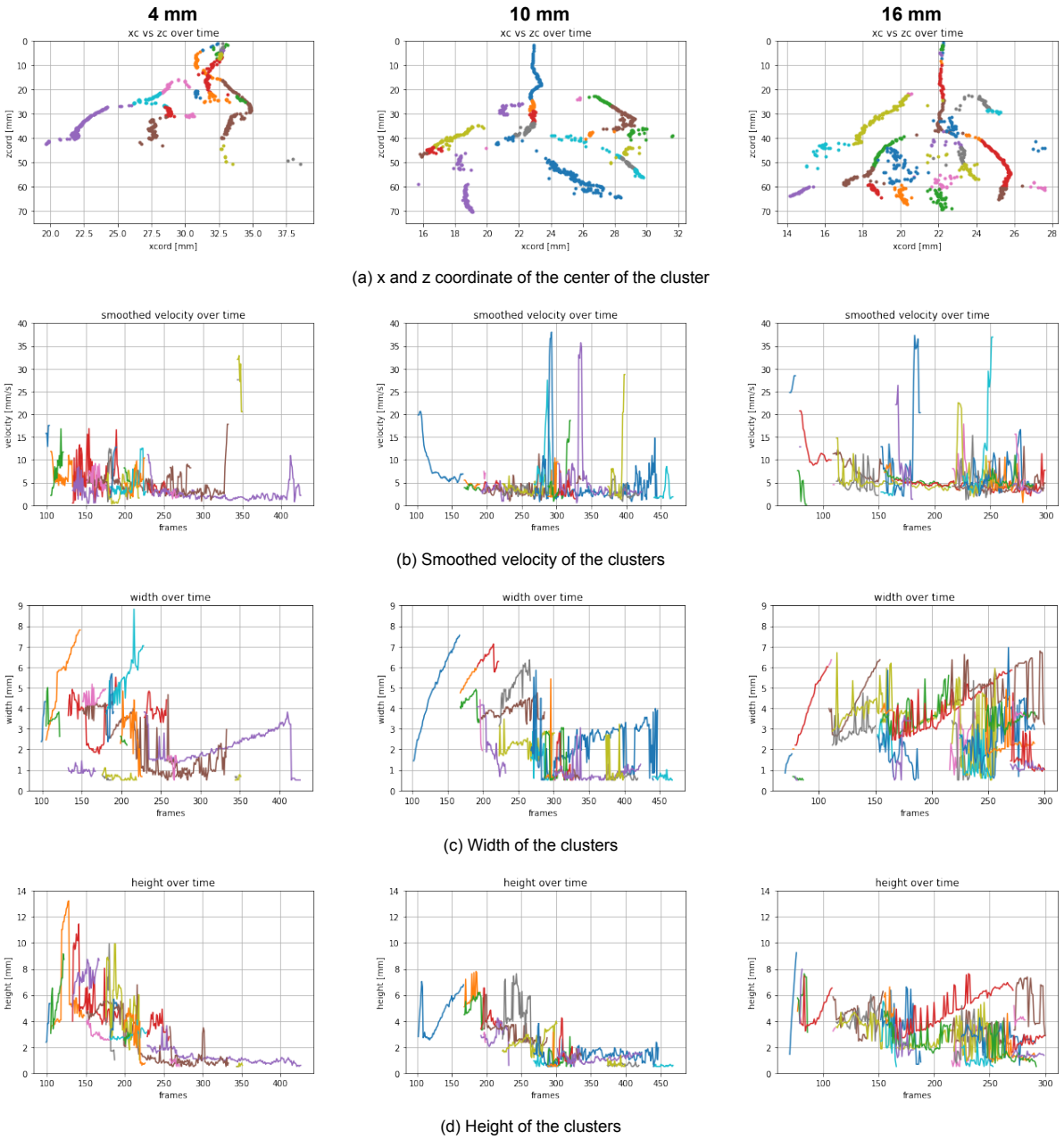

(a) x and z coordinate of the center of the cluster

(b) Smoothed velocity of the clusters

(c) Width of the clusters

(d) Height of the clusters

Figure G.1: Graphs of the results of the preparatory experiments. Left column: $4\,mm$ aperture, center column: $10\,mm$ aperture, right column: $16\,mm$ aperture. Each colour represents a cluster. Note that the scale on x-axis of the figures is not equal.

Cluster center coordinates

The x and z coordinates of the centers of the clusters can be seen in Figure G.1a. It could clearly be seen that under all aperture widths, the clusters bifurcated multiple times and the bifurcated cluster generally continued its path outwards. As a cluster travelled downwards, bulk fluid was entrained in the cluster and what Adachi et al., 1978; Machu et al., 2001 call a *torus* was formed. As the cluster moved further, the ring-shaped torus at some point broke up and the cluster bifurcated. This process repeated and therefore lead to more clusters as the z coordinate increased. Each bifurcation lead to a reduced concentration per cluster and hence, each cluster was less easily identified. Consequently, small changes in colour intensity could change the identified center of the cluster.

This lead to the more scattered center identification as the z coordinate increased, as could also be observed in the graphs. The empty distance between a cluster and its bifurcations could be explained by the fact that a cluster can already be in the process of bifurcation, yet it was still identified as a single cluster by the Mean-Shift algorithm. Only when the cluster had fully bifurcated, a new cluster was identified, but this full bifurcation only occurred a few millimeters away from the continued parent cluster.

The $4\ mm$ aperture showed a distinctive difference compared to the larger apertures, as cluster bifurcation occurred nearly immediately. The early bifurcation lead to a chaotic early phase of cluster development, as indicated by the many identified clusters. As proposed by (Boomsma and Pyrak-Nolte, 2015), this behaviour may be explicable by the increased drag forces of the wall on the cluster, leading to an early bifurcation. Since the cycle of bifurcations started early for the $4\,mm$ aperture, many clusters were identified in the early stage of cluster development. Additionally, the travelled distance of the clusters was smallest of all fracture apertures, which was in agreement with (Boomsma and Pyrak-Nolte, 2015). Although the clusters could be analysed for a total of 352 frames, it should be noted that this was due to a single cluster that was above the set colour intensity threshold and thus could still be identified. The rest of the clusters had already become too diffuse after the many bifurcations that occurred.

The first thing that stood out in the $10\ mm$ aperture was the longevity of the first single cluster that moved down the macro-model. Only after approximately 170 frames, the first cluster bifurcated. Of the three apertures, this was the longest time before first bifurcation occurred. Moreover, the clusters could be identified for the longest duration in the $10\ mm$ aperture (400 frames). This may partially be the reason why these clusters travelled the furthest. Findings of these experiments however could also be explained by the fact that the $10\,mm$ aperture was within the optimal confinement region (Boomsma and Pyrak-Nolte, 2015). In this region, confining forces on the cluster were optimal and bifurcation was suppressed. The drag forces of the wall on the other hand were minimized, resulting in a minimum loss of speed and less bifurcations.

Remarkable for the $16mm$ was the contrast between early and late stage of cluster development and the symmetric development. While the early phase was characterised by only a few clusters, the final phase contained many clusters as a result of bifurcations. It should be noted that the first bifurcation was the result of the fat trail left behind after injection, which was briefly identified. Interestingly, the first real bifurcation was one that split into three, rather than two (at $z \approx 26\ mm$). Similar behaviour was observed at the duplicate tests. The travelled distance was slightly less than, but comparable to, the $10\,mm$ aperture. In addition, the number of frames which could be analysed were quite similar, 230 and 400 for the $16\,mm$ and $10\,mm$ respectively. This may indicate that the behaviour in the $10\,mm$ and $16\ mm$ might not be all too different and velocities were similar. It should however be noted that the clusters travelled the least lateral distance in the $16\ mm$ aperture. One possible explanation may be that the clusters could travel more in the depth plane and consequently travelled less in x-direction.

Cluster velocities

A general remark that needs to made with regard to the initial velocity, is the fact that this velocity was caused by the momentum created by injecting the solution. For all fracture apertures, the smoothed velocity seemed to asymptotically approach a final velocity (Figure G.1b). Also, the smoothed velocity generally showed peaky behaviour. This mainly occurred after multiple bifurcations had already occurred. The diluted clusters could less well be identified and consequently, cluster centers could shift with only small changes in colour intensity. With slightly shifting cluster centers, the distance between centers between frames also became more distorted, thus also affecting the velocity computations.

The smoothed velocity for the $4\ mm$ aperture in particular showed peaky behaviour. This reflects the rapid bifurcations that occurred early on, as explained above. It should be noted that the single cluster at the end was not a single cluster that remained, but rather was the only cluster bright enough to be detected. As with all fracture apertures, the velocity steadily decreased and seemed to reach a stable plateau around $2\ mm/s$. This velocity was a bit lower compared to the wider apertures, which was expected, since the drag forces of the wall decreased cluster velocity.

The $10\ mm$ aperture showed the least peaky behaviour, which was explained by the lower number of bifurcation events that occurred. The terminal velocity of the first cluster was larger than velocities in the rest of the experiment, which may partially be explained by the remainder of injection momentum, but could also be because no bifurcations had yet occurred. As more bifurcations occurred, the velocity showed more flashy peaks, but the general trend seemed to be a stable velocity of around $3\ mm/s$.

The clusters in the $16\ mm$ generally showed similar behaviour to the $10\ mm$ aperture. However, there were slightly more peaks earlier on due to sooner bifurcations. Interesting was the peak-free region from frame 180 up to frame 220. This region was most likely there since the initial bifurcations had passed and a few clear clusters fell steadily through the macro-model. Then, from frame 220 and onward, clusters become so diffuse that identification became hard and the peaks started occurring once again. The terminal velocity in the $16\ mm$ aperture seemed to be similar to the $10\ mm$ aperture, remaining at a stable $5\ mm/s$.

Cluster widths

A clear trend in the width over time could be observed (Figure G.1b). Each cluster had a predominantly increasing width, before the cluster finally was too diffuse to be observed. It should be noted that no clusters under $0.5\,mm$ were detected, as these were discarded in the analysis process to remove noise.

The $4\ mm$ aperture showed a wider initial cluster than the larger apertures, demonstrating that the drag forces of the wall immediately worked on the cluster, tearing it apart. The clusters in this small aperture seemed to be more short-lived and bifurcated quickly, resulting in the width quickly reducing between following clusters. It could well be seen that the process of bifurcation repeated itself, as the width of an individual cluster nearly almost increased, confirming the observation of a drop converting to a torus, which entrains bulk fluid, widens and finally bifurcates (Adachi et al., 1978; Machu et al., 2001).

The persistent initial cluster in the $10\ mm$ aperture was clearly visible and had a steadily increasing width, until it bifurcated. As with the smaller aperture, the width for an individual cluster steadily increased for almost all clusters, whereas the width for all clusters over time reduced. This can be expected since bifurcated clusters contained less material and can therefore develop less wide.

Again, it became clear that the initial development of clusters for the $10\ mm$ and $16\ mm$ aperture were quite similar. In the $16\ mm$ aperture, break-up of the initial rising line up to 100 frames can be attributed to the small bifurcations that were identified by the software. The existing cluster then was assigned a new ID (as explained in Figure 2.10). Interestingly enough, not only did the width of a single clusters increase, but the width of all clusters over time seemed to increase too. This was explained by the fact that it was most likely the same cluster that continued throughout the frames, but got a new ID due to small bifurcations that occurred in the vicinity. It can be seen that from frame 160 and onward, a select group of clusters steadily moved through the macro-model and had a steadily increasing width until they bifurcated some 100 frames, or 2 seconds, later. The sudden rise in bifurcations was also clearly visible in the graph, most likely because of the diffuse clusters that could not well be identified.

Cluster heights

The height of the clusters over time seemed to follow the same trend as the width of the clusters (Figure G.1d). Recall that, similar to the width, clusters with heights smaller than $0.5\,mm$ were discarded in the cluster analysis process to remove unwanted noise. Hence, this set a lower limit of cluster height.

In the $4\ mm$ aperture, the increase in height of each individual cluster was less pronounced than with the width. However, the general trend was clear; the more bifurcations have occurred, the less height the clusters developed. Here, it could be seen once more that many bifurcations had occurred in the early phase, firstly because of the many clusters in the first 100 frames and secondly because the height drastically reduced throughout the frames.

The clusters in the $10\,mm$ aperture showed a more pronounced increase in height for an individual cluster, despite the general trend over all clusters to be a decrease in height. Compared to the smaller aperture, it took a longer time before the height reached a plateau around $1\ mm$. The longevity of the initial cluster allowed a clear observation of its behaviour. It can be seen that the height increased until it bifurcated into a cluster with quite a large height, which can be explained as follows. As the initial cluster travelled downwards, it developed some beginning bifurcations. These bifurcations were not yet far enough away from the parent cluster, resulting in a long-living single cluster. When the clusters finally bifurcated, they were already quite stretched out, resulting in a large height at bifurcation. This process could not only be seen in the $10\ mm$ aperture, but also occurred with the initial cluster in the $16\ mm$ aperture.

Remarkable for the $16\ mm$ aperture was the slow decrease in height over frames. As discussed previously, there were a few selected clusters that persisted throughout the macro-model and therefore had time to develop in z-direction, increasing their height. What was interesting, was the sudden decrease in height of a cluster from frame 260 and onward. Analysing the individual frames gave insight in these results. As the cluster moved downwards, the bottom of the cluster moved faster than the top, resulting in a separation between the top and bottom. The bottom part was identified as the same cluster, losing height, whereas the top was merging with another cluster and diffused quickly after.

Conclusion

These experiments provided evidence that an optimal fracture regime as proposed by (Boomsma and Pyrak-Nolte, 2015) does indeed exist. The clusters in the $4\ mm$ aperture clearly showed more bifurcations, less travelled distance and a rapid increase, followed by a rapid decrease, in height. These may all be indicators for a too narrow fracture aperture, resulting in large drag forces imposed on the cluster. The $10\,mm$ and $16\,mm$ apertures were not all too different, as can be seen in the initial bifurcation pattern, a comparable travelled distance and a generally quite similar height development. There were however some differences, such as the slightly higher terminal velocity of the $16\ mm$ aperture and the strong presence of a few stable clusters. Nevertheless, it could be argued that the 10 and $16\,mm$ apertures were both in a more optimal regime, experiencing less cluster bifurcations and larger travelled distances.

It should be noted that, although these experiments provided insights in fracture apertures, they should be analysed with care. The written python code helped analysing cluster behaviour, but peculiarities arose that had to be manually looked into for explanation. The diffusing of clusters provided challenges for the Mean-Shift algorithm, resulting in flashy peaks or other odd behaviour. So although the cluster analyses provided a good insight in general trends, results should still be looked at with care.

H

Temperature and Injection Volume Measurements

Temperature measurement

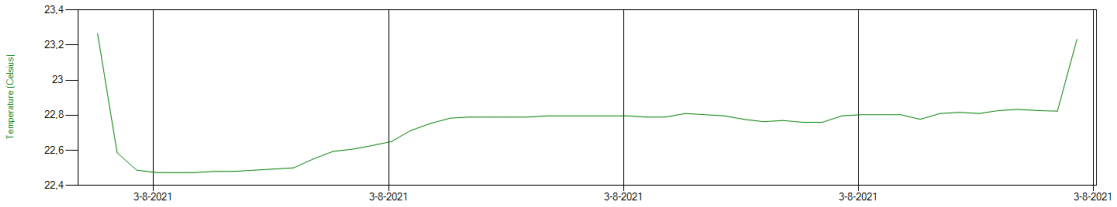

Figure H.1: Temperature data of the top diver

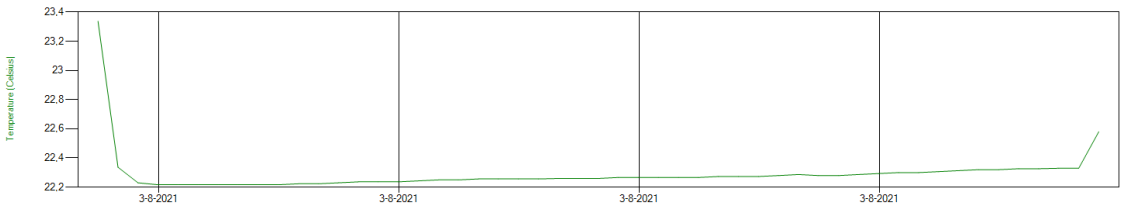

Figure H.2: Temperature data of the bottom diver

The top diver was suspended just beneath the water surface in the tank, whereas the bottom divers was suspended close to the bottom of the tank. Manual temperature measurements of the water at these locations indicated that the top diver should be corrected for -0.3 °C and the bottom diver should be corrected with +0.1 °C. Incorporating these corrections, the temperature difference between the top and bottom of the tank, after all experiments in the series were completed, was approximately 0.1 °C. Increase in water temperature during an experimental series and temperature gradient induced flow was therefore assumed negligible.

Injection volume measurement

Table H.1: Syringe 1

	20 μL	40 μL	60 μL	80 μL	99 μL
Average error (μL)	15.572	30.493	46.049	61.034	75.562
Average error (%)	77.86	76.23	76.75	76.29	76.32
Std. dev of ejected volume (μL)	0.107	0.310	0.233	0.123	0.192

Table H.2: Syringe 2

	20 μL	40 μL	60 μL	80 μL	99 μL
Average error (μL)	15.450	30.529	46.626	60.813	75.149
Average error (%)	77.25	76.32	76.04	76.02	76.91
Std. dev of ejected volume (μL)	0.076	0.214	0.318	0.132	0.188

Table H.3: Syringe 3

	20 μL	40 μL	60 μL	80 μL	99 μL
Average error (μL)	15.414	30.741	46.432	60.004	75.981
Average error (%)	77.07	76.85	76.39	76.25	76.75
Std. dev of ejected volume (μL)	0.646	0.194	1.569	0.158	01.208

Injection accuracy was tested at 5 volumes (20, 40, 60, 80 and 99 μL). Experiments with colloidal swarms were performed with an injection velocity of $40\,\mu L$ displayed on the pump. The injected volume on average differed a staggering 76 %, which was most likely attributed to a setting on the pump that was overlooked. The resulting injected volume during the experiments was thus on average $9.5 \mu L$. Standard deviation of injection volumes however was small and it was assumed that this did not cause the observed difference in velocities between series of experiments.

Bibliography

Adachi, K., Kiriyama, S., & Yoshioka, N. (1978). The behavior of a swarm of particles moving in a viscous fluid. *Chemical Engineering Science*, *33*(1), 115–121.

Beven, K., & Germann, P. (1982). Macropores and water flow in soils. *Water resources research*, *18*(5), 1311–1325.

Boomsma. (2014). *Particle swarms in confining geometries* (Doctoral dissertation). Purdue University.

Boomsma, & Pyrak-Nolte, L. J. (2015). Particle swarms in fractures. *Fluid dynamics in complex fractured-porous systems* (pp. 63–84). American Geophysical Union (AGU).

Bradford, S. A., Bettahar, M., Simunek, J., & Van Genuchten, M. T. (2004). Straining and attachment of colloids in physically heterogeneous porous media. *Vadose Zone Journal*, *3*(2), 384–394.

Bradford, S. A., Yates, S. R., Bettahar, M., & Simunek, J. (2002). Physical factors affecting the transport and fate of colloids in saturated porous media. *Water resources research*, *38*(12), 63–1.

Chassagne, C. (2019). *Introduction to colloid science*. Delft Academic Press.

Collingwood, R. (2021). Ryancollingwood/astar.py. https://gist.github.com/ryancollingwood/32446307e976a11a1185a5394d6657bc

Comaniciu, D., & Meer, P. (2002). Mean shift: A robust approach toward feature space analysis. *IEEE Transactions on pattern analysis and machine intelligence*, *24*(5), 603–619.

Davis, R. H., & Acrivos, A. (1985). Sedimentation of noncolloidal particles at low reynolds numbers. *Annual Review of Fluid Mechanics*, *17*(1), 91–118.

Grace, H. (1971). Dispersion phenomena in high viscosity immiscible fluid systems and applications of static mixers aa dispersion devices in such systems. *Engng Found. 3rd Res. Cmf. Mixing, Andover, New Hampshire*.

Grout, H., Wiesner, M. R., & Bottero, J.-Y. (1999). Analysis of colloidal phases in urban stormwater runoff. *Environmental Science & Technology*, *33*(6), 831–839.

Hadamard, J. (1911). Mouvement permanent lent d'une sphere liquid et visqueuse dans un liquide visqueux. *CR Hebd. Seances Acad. Sci. Paris*, *152*, 1735–1738.

Happel, J., & Brenner, H. (1965). *Low reynolds number hydrodynamics*. Prentice-Hall.

Kjaergaard, C., Moldrup, P., De Jonge, L. W., & Jacobsen, O. H. (2004). Colloid mobilization and transport in undisturbed soil columns. ii. the role of colloid dispersibility and preferential flow. *Vadose Zone Journal*, *3*(2), 424–433.

Leij, F. J., & Bradford, S. A. (2013). Colloid transport in dual-permeability media. *Journal of contaminant hydrology*, *150*, 65–76.

Liao, R., Yang, P., Wu, W., Luo, D., & Yang, D. (2018). A dna tracer system for hydrological environment investigations. *Environmental science & technology*, *52*(4), 1695–1703.

Lin, Y., Tan, J. H., Phan-Thien, N., & Khoo, B. C. (2017). Settling of particle-suspension drops at low to moderate reynolds numbers. *European Journal of Mechanics-B/Fluids*, *61*, 72–76.

Machu, G., Meile, W., Nitsche, L. C., & Schaflinger, U. (2001). Coalescence, torus formation and breakup of sedimenting drops: Experiments and computer simulations. *Journal of Fluid Mechanics*, *447*, 299.

Malenda, M., & Pyrak-Nolte, L. J. (2016). Particle swarm transport across the fracture-matrix interface. *AGU Fall Meeting Abstracts*, *2016*, H53D–1740.

Malvern Instruments Ltd. (2021). *Zeta potential - an introduction in 30 minutes* (tech. rep.). https://warwick.ac.uk/fac/cross_fac/sciencecity/programmes/internal/themes/am2/booking/particlesize/mrk654-01_an_introduction_to_zeta_potential_v3.pdf

McCarthy, J., & Zachara, J. (1989). Es&t features: Subsurface transport of contaminants. *Environmental science & technology*, *23*(5), 496–502.

McDowell-Boyer, L. M., Hunt, J. R., & Sitar, N. (1986). Particle transport through porous media. *Water resources research*, *22*(13), 1901–1921.

Metzger, B., Nicolas, M., & Guazzelli, É. (2007). Falling clouds of particles in viscous fluids. *Journal of Fluid Mechanics*, *580*, 283–301.

Mohanty, S. K., Saiers, J. E., & Ryan, J. N. (2016). Colloid mobilization in a fractured soil: Effect of pore-water exchange between preferential flow paths and soil matrix. *Environmental science & technology*, *50*(5), 2310–2317.

Molnar, I. L., Johnson, W. P., Gerhard, J. I., Willson, C. S., & O'Carroll, D. M. (2015). Predicting colloid transport through saturated porous media: A critical review. *Water Resources Research*, *51*(9), 6804–6845. https://doi.org/https://doi.org/10.1002/2015WR017318

Molnar, I. L., Pensini, E., Asad, M. A., Mitchell, C. A., Nitsche, L. C., Pyrak-Nolte, L. J., Miño, G. L., & Krol, M. M. (2019). Colloid transport in porous media: A review of classical mechanisms and emerging topics. *Transport in Porous Media*, *130*(1), 129–156.

Myłyk, A., Meile, W., Brenn, G., & Ekiel-Jeżewska, M. L. (2011). Break-up of suspension drops settling under gravity in a viscous fluid close to a vertical wall. *Physics of fluids*, *23*(6), 063302.

Nitsche, J., & Batchelor, G. (1997). Break-up of a falling drop containing dispersed particles. *Journal of Fluid Mechanics*, *340*, 161–175.

Paunescu, D., Puddu, M., Soellner, J. O., Stoessel, P. R., & Grass, R. N. (2013). Reversible dna encapsulation in silica to produce ros-resistant and heat-resistant synthetic dna'fossils'. *Nature protocols*, *8*(12), 2440–2448.

Pedregosa, F., Varoquaux, G., Gramfort, A., Michel, V., Thirion, B., Grisel, O., Blondel, M., Prettenhofer, P., Weiss, R., Dubourg, V., Vanderplas, J., Passos, A., Cournapeau, D., Brucher, M., Perrot, M., & Duchesnay, E. (2011). Scikit-learn: Machine learning in Python. *Journal of Machine Learning Research*, *12*, 2825–2830.

Pengel, A. S. (2016). *Cracking up: The influence of water availability on the 3d desiccation crack pattern in kaolin clay* (Master's thesis). Delft University of Technology. https://repository.tudelft.nl/islandora/object/uuid%5C%3Aa20a1f83-7568-4fd8-a4a3-197e856f618b

Rybczynski, W. (1911). Uber die fortschreitende bewegung einer flussigen kugel in einem zahen medium. *Bull. Acad. Sci. Cracovie A*, *1*, 40–46.

Saiers, J. E., Hornberger, G. M., & Harvey, C. (1994). Colloidal silica transport through structured, heterogeneous porous media. *Journal of Hydrology*, *163*(3-4), 271–288.

Savitzky, A., & Golay, M. J. (1964). Smoothing and differentiation of data by simplified least squares procedures. *Analytical chemistry*, *36*(8), 1627–1639.

Seif, G. (2018). The 5 clustering algorithms data scientists need to know. https://towardsdatascience.com/the-5-clustering-algorithms-data-scientists-need-to-know-a36d136ef68

Sharma, A. N., Luo, D., & Walter, M. T. (2012). Hydrological tracers using nanobiotechnology: Proof of concept. *Environmental science & technology*, *46*(16), 8928–8936.

Sirivithayapakorn, S., & Keller, A. (2003). Transport of colloids in saturated porous media: A pore-scale observation of the size exclusion effect and colloid acceleration. *Water Resources Research*, *39*(4).

Stone, H. A. (1994). Dynamics of drop deformation and breakup in viscous fluids. *Annual Review of Fluid Mechanics*, *26*(1), 65–102.

Stumm, W. (1977). Chemical interaction in particle separation. *Environmental Science & Technology*, *11*(12), 1066–1070.

Swift, N. (2020). Nicholas-swift/astar.py. %7Bhttps://gist.github.com/Nicholas-Swift/003e1932ef2804bebef2710527008f44#file-astar-py%7D

Tang, Y., Foppen, J. W., & Bogaard, T. A. (2021). Transport of silica encapsulated dna microparticles in controlled instantaneous injection open channel experiments. *Journal of Contaminant Hydrology*, *242*, 103880.

Weaver, K. (2017). Split-video-by-frame.py. https://gist.github.com/keithweaver/70df4922fec74ea87405b83840b45d57

Yao, K.-M., Habibian, M. T., & O'Melia, C. R. (1971). Water and waste water filtration. concepts and applications. *Environmental science & technology*, *5*(11), 1105–1112.